Induced spin-orbit coupling in twisted graphene–transition metal dichalcogenide heterobilayers: Twistronics meets spintronics

Alessandro David,[1,*] Péter Rakyta,[2] Andor Kormányos,[2,†] and Guido Burkard[1,‡]
[1]*Department of Physics, University of Konstanz, D-78464 Konstanz, Germany*
[2]*Department of Physics of Complex Systems, Eötvös Loránd University, Budapest, Hungary*

(Received 21 May 2019; revised manuscript received 24 July 2019; published 8 August 2019)

We propose an interband tunneling picture to explain and predict the interlayer twist-angle dependence of the induced spin-orbit coupling in heterostructures of graphene and monolayer transition metal dichalcogenides (TMDCs). We obtain a compact analytic formula for the induced valley Zeeman and Rashba spin-orbit coupling in terms of the TMDC band structure parameters and interlayer tunneling matrix elements. We parametrize the tunneling matrix elements with few parameters, which in our formalism are independent of the twist angle between the layers. We estimate the value of the tunneling parameters from existing density functional theory calculations at zero twist angle and we use them to predict the induced spin-orbit coupling at nonzero angles. Provided that the energy of the Dirac point of graphene is close to the TMDC conduction band, we expect a sharp increase of the induced spin-orbit coupling around a twist angle of 18°.

DOI: 10.1103/PhysRevB.100.085412

I. INTRODUCTION

Since its isolation, graphene [1,2] has shown a plethora of interesting phenomena [3]. Among others, long spin-relaxation times [4,5] and spin-diffusion lengths [6] have been observed in graphene, making it a strong candidate for spintronics applications [7]. However, the weak intrinsic spin-orbit coupling (SOC) of graphene [8] hinders the control and tunability of possible spintronics devices. Moreover, a higher SOC in graphene is also desirable to produce, e.g., the quantum spin Hall effect, initially predicted in this material [9], or pseudohelical edge states [10] in zigzag ribbons.

A recent impetus to graphene spintronics has been given by van der Waals engineering [11], i.e., the fabrication of heterostructures of different two-dimensional materials weakly bound by van der Waals forces. These heterostructures can possess functionalities that the individual constituent layers may not have. In order to increase the SOC in graphene, one of the most actively pursued directions is to interface it with materials that have strong intrinsic SOC, such as transition metal dichalcogenides (TMDCs) [12–26]. TMDCs are expected to be good candidates for graphene spintronics for two reasons: (i) it was shown that TMDC substrates do not degrade the mobility of graphene [24,27], and (ii) they host a strong intrinsic SOC of the order of 100 meV (10 meV) in their valence (conduction) band [28] and hence can potentially be suitable materials for proximity-induced SOC. The increase of SOC in graphene would affect its spin-transport properties (see Ref. [29] for a recent review of spin transport in graphene–TMDC heterostrutures). Here, we briefly mention that, e.g., the measurement of weak antilocalization (WAL) [13–15,17,20–22] and the beating of Shubnikov–de Haas oscillations (SdH) [14] proved that SOC is strongly enhanced in graphene–TMDC heterostructures. Details regarding the type and magnitude of the proximity-induced SOC are less clear. Based on WAL measurement, Refs. [15,17] argued that the induced SOC in graphene is of Rashba type which is due to the inversion symmetry-breaking effect of the substrate. The measurements of a large anisotropy of the in-plane and out-of-plane spin-relaxation times [18,25] can be interpreted [30] as an indication that a valley Zeeman type SOC is also induced and its magnitude is comparable to the Rashba type SOC. This is consistent with the data extracted from SdH oscillations [14] and a similar conclusion was also reached in a more recent WAL measurement [21]. These measurements usually employed either bulk or few-layer TMDC substrate. On the other hand, Ref. [22] found that a monolayer TMDC substrate may induce strong Kane-Mele type SOC.

On the theoretical side, density functional theory (DFT) calculations for aligned graphene–TMDC structures [13, 31–34] showed that SOC can be induced in graphene. Direct comparison between these theoretical results and the measurements is not straightforward. First, the DFT band structure calculations are usually fitted with model Hamiltonians for graphene in order to extract the SOC constants and the corresponding energy scales. However, most measurements yield information on spin-relaxation times. Therefore, further information about intervalley scattering times as well as the dominant spin-relaxation mechanisms is needed in order to interpret the observations in terms of SOC energy scales. Second, while most measurements used few-layer TMDCs as substrates, the DFT calculations assumed monolayer TMDCs. It is not entirely clear if the differences in the band structure of monolayer and bulk TMDCs can influence the induced SOC.

*alessandro.david@uni-konstanz.de
†andor.kormanyos@complex.elte.hu
‡guido.burkard@uni-konstanz.de

Third, in contrast to the theoretical calculations, in the experiments the layers were not intentionally aligned and in general there is most likely to be a twist angle between them, as observed in Ref. [35]. (We note that Refs. [36,37] performed calculations for a few twist angles where the graphene and TMDC layers form approximately commensurate structures, but the SOC was not taken into account). The tight-binding (TB) models of Refs. [38,39] considered aligned structures or small twist angles. Only very recently was the TB methodology extended to the calculation of induced SOC for arbitrary twist angle between graphene and the TMDC substrate [40].

Here, we use an approach that describes the induced SOC in terms of virtual band-to-band tunneling between graphene and the monolayer TMDC substrate. This perturbative approach is motivated by previous DFT calculations [13,31–34,36,37] which show that the linear dispersion of graphene close to the Dirac point is preserved because the interaction between the layers is rather weak. In real space, we take into account tunneling processes between graphene and the closest layer of chalcogen atoms in the TMDC. This approximation allows to obtain a simple and effective parametrization of the interlayer tunneling using just two real parameters. We show how these parameters can be applied to describe tunneling for all twist angles. We then calculate the induced valley Zeeman and Rashba type SOC in graphene as a function of interlayer twist angle and demonstrate the close relation between the intrinsic properties of the substrate and the induced SOC in graphene. As a concrete example, we consider graphene on monolayer MoS_2, but the same approach can be used for other semiconductor monolayer TMDC where the Dirac point of graphene is in the band gap of the substrate. The possibility to tune the strength of the induced SOC in graphene by changing the interlayer twist angle links graphene spintronics with the newly emerging field of twistronics [41–44].

This paper is organized as follows. In Sec. II we present the details of the heterostructure. In Sec. III we describe the tunneling between the two layers and we introduce the idea of tunneling to a band. We construct a Hamiltonian for the Dirac points of graphene in Sec. IV and we indicate how valley Zeeman and Rashba type SOC are induced in graphene by the TMDC substrate in Secs. V and VI, respectively. We present and discuss our result in Sec. VII and we draw our conclusions in Sec. VIII.

II. TWISTED HETEROSTRUCTURE

Graphene [1–3] and monolayer TMDCs [28,45,46] share the same two-dimensional (2D) hexagonal structure given by two triangular sublattices A and B. For graphene the lattice constant is $a_G = 2.46$ Å and the two sublattices are occupied by carbon atoms. Conduction and valence bands of graphene show conic dispersion relations at the two inequivalent corners of the Brillouin zone $\boldsymbol{K}_\tau = \tau \boldsymbol{K} = 4\pi/3a_G(\tau, 0)$, with $\tau = \pm 1$, also known as Dirac points. A two-band nearest-neighbor tight-binding (TB) model that takes into account only one p_z orbital per carbon atom leads to the Hamiltonian [3]

$$h^{\mathrm{gr}}_{\tau \boldsymbol{K}}(\boldsymbol{k}) = \hbar v_F(\tau k_x \sigma_x + k_y \sigma_y), \tag{1}$$

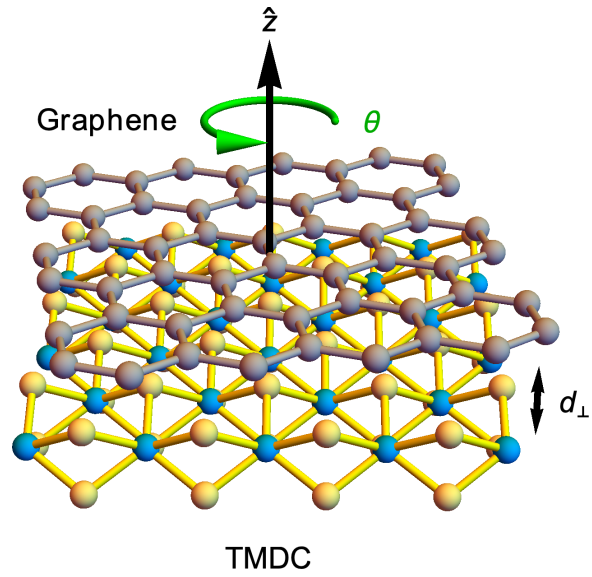

FIG. 1. 3D view of graphene on top of monolayer TMDC. Here, θ is the twist angle between graphene and the TMDC layer, while $d_\perp$ is the perpendicular distance between graphene and the upper (closest) chalcogen layer of the TMDC.

where $|\boldsymbol{k}| \ll |\boldsymbol{K}|$, σ_x and σ_y are Pauli matrices for the sublattice pseudospin and v_F is the Fermi velocity of the electrons. Monolayer TMDCs have larger lattice constants than graphene ($a_T = 3.1$–3.3 Å), therefore smaller Brillouin zones. The metal atoms occupy the A sublattice sites, while the chalcogen atoms are found on the B sublattice sites but vertically shifted by $\pm d_{X\text{-}X}/2$, where $d_{X\text{-}X}$ is the chalcogen-chalcogen distance [28]. We consider a heterobilayer van der Waals structure formed by graphene deposited on top of monolayer TMDC. The graphene layer is separated by $d_\perp$ from the topmost TMDC chalcogen layer (see Fig. 1). Because of the lattice constant difference between graphene and the TMDC they do not form a commensurate structure. In general, the graphene lattice vectors can be rotated by angle θ with respect to the TMDC lattice vectors and the A sublattice of graphene may be shifted horizontally with respect to the A sublattice of the TMDC by vector $\boldsymbol{r}_0$. [The vector $\boldsymbol{r}_0$ is contained in the first (rotated) unit cell of graphene.] In the rest of the paper, we use the following notations: primed quantities are related to the TMDC and every vector $\boldsymbol{r}$ that is rotated by an angle θ with respect to its original definition is indicated by $\boldsymbol{r}^\theta = R(\theta)\boldsymbol{r}$, where R is the rotation operator around the z axis. The sublattice sites are found at the positions $\boldsymbol{R}^\theta_X = n_1\boldsymbol{a}^\theta_1 + n_2\boldsymbol{a}^\theta_2 + \boldsymbol{\tau}^\theta_X + \boldsymbol{r}_0$, $\boldsymbol{R}_{X'} = n'_1\boldsymbol{a}'_1 + n'_2\boldsymbol{a}'_2 + \boldsymbol{\tau}_{X'}$, where $X = A, B$ and $X' = A', B'$ refer to the graphene and TMDC sublattice, respectively. Here, $\boldsymbol{a}_{1,2}$ ($\boldsymbol{a}'_{1,2}$) are the primitive lattice vectors of graphene (TMDC) and $\boldsymbol{\tau}_X$ ($\boldsymbol{\tau}_{X'}$) indicates the position of sublattice X (X') in the unit cell. See Appendix A for the explicit definitions used in this work.

III. INTERLAYER TUNNELING

Looking at the *ab initio* calculations of Refs. [13,33], the Dirac point of graphene is located inside the TMDC band gap and its linear dispersion is mostly unaffected. However,

modifications of the graphene bands very close to the Dirac point indicate spin-orbit splittings and possibly the presence of a spin-independent band-gap opening as well. We will use perturbation theory to give a microscopic description of the induced spin splitting of the graphene bands.

The total Hamiltonian has three parts, describing the isolated eigenstates of graphene and TMDC and the interlayer tunneling, respectively, $H_{\rm tot} = H_{\rm gr} + H_{\rm TMDC} + H_{\rm T}$. The theory for interlayer interactions in incommensurate atomic layers [47] gives a compact analytic form, in momentum space, for the interlayer tunneling matrix elements $U_{XX'}(\boldsymbol{k},\boldsymbol{k}') = {}_{\rm gr}\langle X,\boldsymbol{k}^\theta|\,H_{\rm T}\,|X',\boldsymbol{k}'\rangle_{\rm TMDC}$ between unperturbed graphene and TMDC states. Here, X and X' run over the sublattice indices and, in general, also over all the atomic orbitals located on the same sublattice site. If there is only one atomic orbital per lattice site, the Bloch states read as $|X,\boldsymbol{k}^\theta\rangle_{\rm gr} = N^{-1/2}\sum_{\boldsymbol{R}_X^\theta} e^{i\boldsymbol{k}^\theta\cdot\boldsymbol{R}_X^\theta}\,|\boldsymbol{R}_X^\theta\rangle$ and $|X',\boldsymbol{k}'\rangle_{\rm TMDC} = N'^{-1/2}\sum_{\boldsymbol{R}_{X'}} e^{i\boldsymbol{k}'\cdot\boldsymbol{R}_{X'}}\,|\boldsymbol{R}_{X'}\rangle$ and the theory gives [41,47,48]

$$U_{XX'}(\boldsymbol{k},\boldsymbol{k}') = \sum_{\boldsymbol{G},\boldsymbol{G}'} \delta_{\boldsymbol{k}^\theta+\boldsymbol{G}^\theta,\boldsymbol{k}'+\boldsymbol{G}'}\; t_{X'}(\boldsymbol{k}'+\boldsymbol{G}') \times e^{i\boldsymbol{G}^\theta\cdot(\boldsymbol{\tau}_X^\theta+\boldsymbol{r}_0)-i\boldsymbol{G}'\cdot\boldsymbol{\tau}_{X'}}, \tag{2}$$

where $\boldsymbol{G}$, $\boldsymbol{G}'$ are reciprocal lattice vectors of graphene and TMDC, respectively. The term $\delta_{\boldsymbol{k}^\theta+\boldsymbol{G}^\theta,\boldsymbol{k}'+\boldsymbol{G}'}$ expresses quasimomentum conservation. In the derivation of Eq. (2) the Slater-Koster two-center approximation [49] has been used, whereby $\langle\boldsymbol{R}_X^\theta|\,H_{\rm T}\,|\boldsymbol{R}_{X'}\rangle = T_{XX'}(\boldsymbol{R}_X^\theta - \boldsymbol{R}_{X'})$ and the tunneling strength in momentum space $t_{X'}(\boldsymbol{q})$ is the Fourier transform of $T_{XX'}(\boldsymbol{R})$. As we consider only one p_z orbital per carbon atom and we adopt the Slater-Koster approximation, $t_{X'}(\boldsymbol{q})$ is insensitive to the graphene sublattice index X (see Appendix B).

Considering now the graphene on monolayer TMDC heterostructure, in real space an electron from graphene may tunnel to any of the three layers of atoms of the TMDC. However, the probability to reach the second or the third atomic layers of the monolayer TMDC is exponentially suppressed with respect to reaching the first, closest one. Therefore, to describe the tunneling we consider only the first (upper) chalcogen layer that is closer to graphene. In contrast to graphene, monolayer TMDCs have a rather complicated band structure. Since DFT calculations indicate that the Dirac point of graphene is found inside the band gap of the TMDC, we expect that the most important bands of the TMDC are those nearest in energy, namely, the conduction and the valence bands. These bands are mainly formed by metal atom d orbitals, but the weights of chalcogen atom p orbitals are nonzero [28]. It follows that the nearest chalcogen layer approximation for tunneling can be used in combination with the band description of the TMDC. Accordingly, we need to extend the theory of Ref. [47] to consider tunneling not from atomic orbital to atomic orbital, but from orbital to an energy band.

The state of an electron in band b of the TMDC can be written as a linear combination of single orbital Bloch states $|b,\boldsymbol{k}'\rangle_{\rm TMDC} = \sum_{X'} c_{bX'}(\boldsymbol{k}')\,|X',\boldsymbol{k}'\rangle_{\rm TMDC}$. Here, the complex amplitudes $c_{bX'}(\boldsymbol{k}')$ are different for each band b. Since we assume that the tunneling to the d orbitals is exponentially suppressed, this sum runs over the three p orbitals of the nearest chalcogen layer and $\boldsymbol{\tau}_{X'} = \boldsymbol{\tau}_{B'}$ when computing the interlayer tunneling matrix. The formalism can be extended in a straightforward way to include the tunneling to the metal atoms' d orbitals as well, but this would lead to several more parameters to fit. As we will show in Sec. VII, using the above approximation our calculations are already in good qualitative agreement with previously known results. We introduce the interlayer tunneling matrix element between orbital X of graphene and band b of the TMDC as $U_{Xb}(\boldsymbol{k},\boldsymbol{k}') = {}_{\rm gr}\langle X,\boldsymbol{k}^\theta|\,H_{\rm T}\,|b,\boldsymbol{k}'\rangle_{\rm TMDC}$. As a consequence, $t_{X'}(\boldsymbol{k}'+\boldsymbol{G}')$ in Eq. (2) is replaced by $t_b(\boldsymbol{k}'+\boldsymbol{G}')$, the band tunneling strength,

$$t_b(\boldsymbol{k}'+\boldsymbol{G}') = \sum_{X'} c_{bX'}(\boldsymbol{k}')\,t_{X'}(\boldsymbol{k}'+\boldsymbol{G}'). \tag{3}$$

IV. BILAYER HAMILTONIAN

We expect $|t_b(\boldsymbol{q})|$ to decay very fast in $|\boldsymbol{q}|$ [41,47,48], therefore, we consider only vectors $\boldsymbol{k}'$ in the TMDC BZ that respect the quasimomentum conservation of Eq. (2), i.e., $\tau\boldsymbol{K}^\theta + \boldsymbol{G}^\theta = \boldsymbol{k}' + \boldsymbol{G}'$, and such that $|\boldsymbol{k}'+\boldsymbol{G}'|$ is minimum. We find that these two conditions are satisfied for three distinct points $\tau\boldsymbol{k}'_j$, $j=1,2,3$, of the TMDC Brillouin zone (BZ), for a fixed value of τ. This is similar to what happens for rotated bilayer graphene [41]. When $\theta\in[0,\pi/3]$, for our choice of reciprocal lattice vectors, these three points are

$$\begin{aligned}\tau\boldsymbol{k}'_1 &= \tau(\boldsymbol{K}^\theta - \boldsymbol{b}'_1),\\ \tau\boldsymbol{k}'_2 &= \tau\left(\boldsymbol{K}^\theta + \boldsymbol{b}^\theta_2 - \boldsymbol{b}'_2\right),\\ \tau\boldsymbol{k}'_3 &= \tau\left(\boldsymbol{K}^\theta - \boldsymbol{b}^\theta_1 + \boldsymbol{b}'_1 + \boldsymbol{b}'_2\right),\end{aligned} \tag{4}$$

where $\boldsymbol{b}_{1,2}$ ($\boldsymbol{b}'_{1,2}$) are the primitive reciprocal lattice vectors of graphene (TMDC). (See Fig. 2 and Appendix A.) Then, one can show (see Appendices B and C) that the band tunneling strength in Eq. (3) can be parametrized by two real numbers $t_\parallel$ and $t_\perp$:

$$t_b(\tau\boldsymbol{K}^\theta) = i\tau[c_{bx}(\tau\boldsymbol{k}'_1)\cos\theta + c_{by}(\tau\boldsymbol{k}'_1)\sin\theta]\,t_\parallel + c_{bz}(\tau\boldsymbol{k}'_1)\,t_\perp, \tag{5}$$

where the connection between the Dirac point $\tau\boldsymbol{K}^\theta$ and the first backfolded point $\tau\boldsymbol{k}'_1$ is given in Eq. (4). We estimate $t_\parallel \approx t_\perp \approx 100$ meV (see Appendix E for details). In order to compute the band tunneling strength for all twist angles θ, Eq. (5) requires the knowledge of the orbital amplitudes $c_{bp}(\tau\boldsymbol{k}'_j)$, $p=x,y,z$, which are intrinsic properties of the TMDC. We have obtained their values for MoS_2 from the tight-binding model of Ref. [50].

One can then set up a bilayer Hamiltonian valid for a neighborhood of the Dirac point $\tau\boldsymbol{K}$ that describes the hybridization with the TMDC:

$$\mathcal{H} = \left(\begin{array}{c|ccc} h^{{\rm gr},\theta}_{\tau\boldsymbol{K}}(\delta\boldsymbol{k}) & T_{\tau\boldsymbol{k}'_1} & T_{\tau\boldsymbol{k}'_2} & T_{\tau\boldsymbol{k}'_3}\\ \hline T^\dagger_{\tau\boldsymbol{k}'_1} & h^{\rm TMDC}_{\tau\boldsymbol{k}'_1}(\delta\boldsymbol{k}) & 0 & 0\\ T^\dagger_{\tau\boldsymbol{k}'_2} & 0 & h^{\rm TMDC}_{\tau\boldsymbol{k}'_2}(\delta\boldsymbol{k}) & 0\\ T^\dagger_{\tau\boldsymbol{k}'_3} & 0 & 0 & h^{\rm TMDC}_{\tau\boldsymbol{k}'_3}(\delta\boldsymbol{k}) \end{array}\right). \tag{6}$$

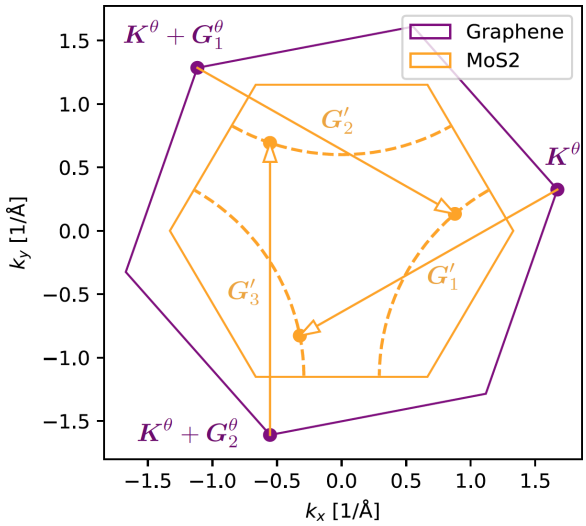

FIG. 2. Backfolded TMDC BZ vectors satisfying the quasimomentum conservation of Eq. (4) for the rotated Dirac point of graphene $\boldsymbol{K}^\theta$. The dashed lines indicate the full paths of the backfolded vectors in the range of twist angles $\theta \in [0, \pi/3]$. Moreover, $\boldsymbol{G}_{1,2}^\theta$ are rotated reciprocal lattice vectors of graphene, while $\boldsymbol{G}_{1,2,3}'$ are reciprocal lattice vectors of the TMDC. As an example, here we have shown in orange the BZ of MoS_2 (with lattice constant $a_T = 3.15$ Å).

Here, $\delta\boldsymbol{k}$ is a small displacement, $|\delta\boldsymbol{k}| \ll |\boldsymbol{K}|$, from the backfolded vectors $\tau\boldsymbol{k}_j'$. The displacement from the Dirac point is therefore $\delta\boldsymbol{k}^{\alpha=-\theta}$ in graphene's coordinate system. The rotated graphene Hamiltonian reads as

$$h_{\tau\boldsymbol{K}}^{\mathrm{gr},\theta}(\delta\boldsymbol{k}) = \hbar v_F \tau |\delta\boldsymbol{k}| \begin{pmatrix} 0 & e^{-i\tau(\varphi_{\delta\boldsymbol{k}}-\theta)} \\ e^{i\tau(\varphi_{\delta\boldsymbol{k}}-\theta)} & 0 \end{pmatrix} \otimes \mathbb{1}_S, \quad (7)$$

with $\varphi_{\delta\boldsymbol{k}} = \arctan(\delta\boldsymbol{k}_x/\delta\boldsymbol{k}_y)$ and $\mathbb{1}_S$ is the identity matrix for the spin degree of freedom. Moreover, $h_{\tau\boldsymbol{k}_j'}^{\mathrm{TMDC}}(\delta\boldsymbol{k})$ describes the Hamiltonian of the TMDC at a vector $\delta\boldsymbol{k}$ distance from $\tau\boldsymbol{k}_j'$. In the simplest case $h_{\tau\boldsymbol{k}_j'}^{\mathrm{TMDC}}(\delta\boldsymbol{k})$ contains the dispersion of those bands that we take into account, e.g., valence and conduction bands. The dispersion of the bands can be obtained, e.g., using the $k \cdot p$ method (see Appendix D) or taken from TB calculations. In our case $h_{\tau\boldsymbol{k}_j'}^{\mathrm{TMDC}}(\delta\boldsymbol{k})$ also includes the effects of the intrinsic SOC of the TMDC on the band structure (see Appendix F). The dispersion of the bands for the TMDC Hamiltonians $h_{\tau\boldsymbol{k}_{2,3}'}^{\mathrm{TMDC}}(\delta\boldsymbol{k})$ can be obtained from $h_{\tau\boldsymbol{k}_1'}^{\mathrm{TMDC}}(\delta\boldsymbol{k})$ because the points $\tau\boldsymbol{k}_j'$ have C_3 symmetry with respect to the Γ point of the TMDC BZ. Therefore,

$$\begin{aligned} h_{\tau\boldsymbol{k}_2'}^{\mathrm{TMDC}}(\delta\boldsymbol{k}) &= h_{\tau\boldsymbol{k}_1'}^{\mathrm{TMDC}}(\delta\boldsymbol{k}^{\alpha=-2\pi/3}), \\ h_{\tau\boldsymbol{k}_3'}^{\mathrm{TMDC}}(\delta\boldsymbol{k}) &= h_{\tau\boldsymbol{k}_1'}^{\mathrm{TMDC}}(\delta\boldsymbol{k}^{\alpha=+2\pi/3}). \end{aligned} \quad (8)$$

Finally, the tunneling from the $\tau\boldsymbol{K}^\theta$ point of graphene to the $\tau\boldsymbol{k}_j'$ points of the TMDC BZ is given by the interlayer tunneling matrices $T_{\tau\boldsymbol{k}_j'}$. In our approximation, the tunneling matrices do not depend on the value of the small wave vector $\delta\boldsymbol{k}$. Using Eqs. (2) and (3), for each band b of the TMDC that we take into account in $h_{\boldsymbol{k}_j'}^{\mathrm{TMDC}}(\delta\boldsymbol{k})$ the corresponding column of the tunneling matrix $T_{\tau\boldsymbol{k}_j'}$ reads as

$$(T_{\tau\boldsymbol{k}_j'})_b = e^{-i\tau\boldsymbol{G}_j'\cdot\boldsymbol{\tau}_{B'}} e^{i\tau\boldsymbol{G}_j^\theta\cdot\boldsymbol{r}_0} t_b(\tau\boldsymbol{K}^\theta) \begin{pmatrix} 1 \\ e^{i\tau\phi_j} \end{pmatrix}, \quad (9)$$

where $\boldsymbol{G}_j = 0, \boldsymbol{b}_2, -\boldsymbol{b}_1$ and $\boldsymbol{G}_j' = \boldsymbol{b}_1', \boldsymbol{b}_2', -\boldsymbol{b}_1' - \boldsymbol{b}_2'$ for $j = 1, 2, 3$, moreover $\phi_j = \boldsymbol{G}_j \cdot \boldsymbol{\tau}_B = 0, 2\pi/3, -2\pi/3$. We assume that $T_{\tau\boldsymbol{k}_j'}$ preserves the spin degree of freedom and therefore it is diagonal in the spin space.

V. VALLEY ZEEMAN SOC

In order to gain further understanding of how the intrinsic properties of the monolayer TMDC determine the induced valley Zeeman type SOC, we apply a Schrieffer-Wolff transformation [51,52] to Eq. (6) to derive an effective graphene Hamiltonian. Following Ref. [53], within second order the correction to the graphene Hamiltonian reads as

$$\delta H_{Xs,X's}^{\mathrm{gr},\tau} = \sum_{j,b} \frac{(T_{\tau\boldsymbol{k}_j'})_{X,b} (T_{\tau\boldsymbol{k}_j'}^\dagger)_{b,X'}}{E_D^{\mathrm{gr}} - E_{bs}^{\mathrm{TMDC}}(\tau\boldsymbol{k}_j' + \delta\boldsymbol{k})}, \quad (10)$$

where $X, X' = A, B$ refers to the graphene sublattices, $s = \uparrow, \downarrow$ is the spin index, $j = 1, 2, 3$, and b is the band index. Moreover, E_D^{gr} is the energy of the Dirac point that we fix, without the loss of generality, to $E_D^{\mathrm{gr}} = 0$, while $E_{bs}^{\mathrm{TMDC}}(\tau\boldsymbol{k}_j' + \delta\boldsymbol{k})$ is the energy of the TMDC band b, spin index s, at the BZ point $\tau\boldsymbol{k}_j' + \delta\boldsymbol{k}$. We remark that Eq. (10) does not describe spin-flip processes ($\delta H_{X\uparrow,X'\downarrow}^{\mathrm{gr},\tau} = 0$) because the tunneling matrices of Eq. (9) are spin preserving. One can make use of the threefold rotational symmetry to simplify Eq. (10) (see Appendix D). Expanding E_{bs}^{TMDC} up to linear terms in $\delta\boldsymbol{k}$, it turns out that the diagonal matrix elements $\delta H_{Xs,Xs}^{\mathrm{gr},\tau}$ are $\delta\boldsymbol{k}$ independent:

$$\delta H_{Xs,Xs}^{\mathrm{gr},\tau} = -3 \sum_b \frac{|t_b(\tau\boldsymbol{K}^\theta)|^2}{E_b(\boldsymbol{k}_1') + s\tau\Delta_{0,b}(\boldsymbol{k}_1')}, \quad (11)$$

where $E_b(\boldsymbol{k}_1')$ is the energy of the TMDC band b (ignoring SOC) at $\boldsymbol{k}_1'$, computed with respect to the Dirac point of graphene and $\Delta_{0,b}(\boldsymbol{k}_1')$ is the spin splitting of band b at $\boldsymbol{k}_1'$ due to the diagonal part of the intrinsic SOC of the TMDC [28]. Equation (11) describes two twist-angle-dependent effects: (i) a spin-independent shift of the Dirac point with respect to TMDC bands and, (ii) a spin splitting of the graphene bands. The latter can be described by the Hamiltonian $H_{\mathrm{VZ}} = \lambda_{\mathrm{VZ}}\, \tau s_z$, where s_z is a Pauli matrix for spin. We follow the notation of Ref. [30] where the Hamiltonian term H_{VZ} describes the induced valley Zeeman SOC. This corresponds to the intrinsic SOC Hamiltonian of Ref. [33] with $\lambda_{\mathrm{I}}^{\mathrm{A}} = -\lambda_{\mathrm{I}}^{\mathrm{B}} = \lambda_{\mathrm{VZ}}$ or to the staggered intrinsic SOC model of Ref. [10] with $\lambda_{\mathrm{I}} = \lambda_{\mathrm{VZ}}$. We find that the constant λ_{VZ} is given by

$$\lambda_{\mathrm{VZ}} = 3 \sum_b \frac{|t_b(\tau\boldsymbol{K}^\theta)|^2 \Delta_{0,b}(\boldsymbol{k}_1')}{E_b^2(\boldsymbol{k}_1') - \Delta_{0,b}^2(\boldsymbol{k}_1')}. \quad (12)$$

This is the first important result of our work. It shows explicitly how λ_{VZ} depends on the intrinsic properties of the TMDC substrate and the twist angle θ between the layers. The latter determines the wave number $\boldsymbol{k}_1'$ and affects the tunneling strength $t_b(\tau\boldsymbol{K}^\theta)$ through Eq. (5). We note that in

this second-order perturbation theory no staggered sublattice potential leading to a spin-independent band gap is obtained.

The off-diagonal matrix elements $\delta H^{\mathrm{gr},\tau}_{As,Bs}(\delta\boldsymbol{k})$ in Eq. (10) are $\delta\boldsymbol{k}$ dependent:

$$\delta H^{\mathrm{gr},\tau}_{As,Bs}(\delta\boldsymbol{k}) = \frac{3}{2}\left(\sum_b \frac{w_{bs\tau,\tau}(\boldsymbol{k}'_1)|t_b(\tau\boldsymbol{K}^\theta)|^2}{E^2_{bs\tau}(\boldsymbol{k}'_1)}\right)[\tau\delta k_x - i\delta k_y], \tag{13}$$

where $E_{bs\tau}(\boldsymbol{k}'_1) = E_b(\boldsymbol{k}'_1) + s\tau\Delta_{0,b}(\boldsymbol{k}'_1)$ and $w_{bs\tau,\tau}(\boldsymbol{k}'_1)$ is a complex quantity related to the local slope of the TMDC band b (see Appendix D). Equation (13) gives a correction to the Fermi velocity of pristine graphene. The proximity-corrected Fermi velocity is

$$\widetilde{v}_F = \left| v_F + e^{i\tau\theta}\frac{3}{2\hbar}\sum_b \frac{w_{bs\tau,\tau}(\boldsymbol{k}'_1)|t_b(\tau\boldsymbol{K}^\theta)|^2}{E^2_{bs\tau}(\boldsymbol{k}'_1)}\right|. \tag{14}$$

We have numerically computed this correction for a pristine graphene Fermi velocity $v_F = 10^6$ m/s, using MoS_2 as the TMDC compound. The correction we find is in the order of $\pm 0.2\%$ depending on the twist angle. In general, the value of v_F is more sensitive to the dielectric constant of the environment [54], therefore, we will not discuss this effect further.

VI. RASHBA TYPE SOC

As already mentioned, WAL measurements suggest that a Rashba type SOC is also induced in graphene. Traditionally, the Rashba SOC in graphene was understood in terms of a symmetry-breaking effect of a perpendicular electric field [7,8,55]. More generally, one can expect that Rashba type SOC is induced when structural asymmetry is present in the heterostructure. Indeed, the DFT calculation of Ref. [33] indicated that even for zero external electric field a finite Rashba SOC is induced in graphene. To our knowledge, the microscopic mechanisms giving rise to the induced Rashba SOC has not yet been discussed. We show that an important contribution comes from virtual interlayer tunneling processes that are facilitated by the off-diagonal spin-flipping elements of the intrinsic SOC matrix of the monolayer TMDC, indicated by $(H_{\mathrm{soc}})_{b\uparrow,b'\downarrow}$ and $(H_{\mathrm{soc}})_{b\downarrow,b'\uparrow}$. Such off-diagonal matrix elements are allowed between pairs of bands if one of the bands is symmetric (even) and the other one is antisymmetric (odd) with respect to reflection on the horizontal mirror plane of the TMDC (see, e.g., Ref. [56] for further discussion of the SOC in monolayer TMDCs). In third-order perturbation theory one finds the following matrix elements [53]:

$$\begin{aligned}\left(\delta H^{\mathrm{gr},\tau}_{\mathrm{R}}\right)_{X\uparrow,X'\downarrow} &= \sum_{j,b,b'} \frac{\left(T_{\tau\boldsymbol{k}'_j}\right)_{X,b}(H_{\mathrm{soc}})_{b\uparrow,b'\downarrow}(T^\dagger_{\tau\boldsymbol{k}'_j})_{b',X'}}{\left[E^{\mathrm{gr}}_D - E^{\mathrm{TMDC}}_b(\tau\boldsymbol{k}'_j)\right]\left[E^{\mathrm{gr}}_D - E^{\mathrm{TMDC}}_{b'}(\tau\boldsymbol{k}'_j)\right]}\end{aligned} \tag{15}$$

and $(\delta H^{\mathrm{gr},\tau}_{\mathrm{R}})_{X\downarrow,X'\uparrow}$ is analogously defined. Here, $b \neq b'$ is the band index and in the denominator we have neglected the dependence of the TMDC band energies $E^{\mathrm{TMDC}}_b(\tau\boldsymbol{k}'_j)$ on the intrinsic SOC [cf. Eq. (10)] because it would lead to higher-order effects. The matrix elements $(H_{\mathrm{soc}})_{b\uparrow,b'\downarrow}$ can be calculated using the TB model of Ref. [50], while the tunneling matrices $(T_{\tau\boldsymbol{k}'_j})_{X,b}$ and $(T^\dagger_{\tau\boldsymbol{k}'_j})_{b',X'}$ can be obtained in the same way as explained in Sec. IV. As we show in Appendix F, each pair of even and odd bands leads to a Rashba SOC strength

$$\lambda_{\mathrm{R},eo} = \frac{6\gamma_d|T_{e,o}(\boldsymbol{K}^\theta)||\Lambda_1(\boldsymbol{k}'_1)|}{\left[E^{\mathrm{gr}}_D - E^{\mathrm{TMDC}}_e(\boldsymbol{k}'_1)\right]\left[E^{\mathrm{gr}}_D - E^{\mathrm{TMDC}}_o(\boldsymbol{k}'_1)\right]} \tag{16}$$

and to a complex phase factor $e^{i\vartheta_{eo}}$, where $\vartheta_{eo} = \mathrm{Arg}[\Lambda_1(\boldsymbol{k}'_1)]$. Here, γ_d is the atomic SOC strength of the metal atoms' d orbitals of the TMDC, $T_{e,o}(\boldsymbol{K}^\theta) = t_e(\boldsymbol{K}^\theta)t^*_o(\boldsymbol{K}^\theta)$, with t_b defined in Eq. (5) and Λ_1 is a complex quantity formed by the SOC matrix elements of the TMDC. We give the explicit definition of Λ_1 as well as the details of the calculations leading to Eq. (16) in Appendix F. To obtain the total Rashba SOC strength, one has to sum over all possible pairs of even and odd bands, including the complex phase factors $e^{i\vartheta_{eo}}$. Therefore, one has

$$\begin{aligned}\lambda_{\mathrm{R,tot}} &= \left|\lambda_{\mathrm{R},e_1o_1}e^{i\vartheta_{e_1o_1}} + \lambda_{\mathrm{R},e_2o_2}e^{i\vartheta_{e_2o_2}} + \cdots\right|,\\ \vartheta_{\mathrm{tot}} &= \mathrm{Arg}\left[\lambda_{\mathrm{R},e_1o_1}e^{i\vartheta_{e_1o_1}} + \lambda_{\mathrm{R},e_2o_2}e^{i\vartheta_{e_2o_2}} + \cdots\right].\end{aligned} \tag{17}$$

In the end one finds that the induced Rashba type SOC in graphene reads as $H_{\mathrm{R}} = (\lambda_{\mathrm{R,tot}}/2)\,e^{-i\vartheta_{\mathrm{tot}}s_z/2}(\tau\sigma_x s_y - \sigma_y s_x)e^{i\vartheta_{\mathrm{tot}}s_z/2}$, where s_x, s_y are spin Pauli matrices. As one can see from Eq. (16) the induced Rashba type SOC, similarly to the induced valley Zeeman SOC, is a second-order process in the interlayer tunneling, but in addition it involves a spin-flip process within the monolayer TMDC. We show the results of our numerical calculations for λ_{R} in Fig. 5. Up to third order of perturbation theory we did not find processes that would lead to a term similar to the Kane-Mele type SOC. Therefore, the total effective graphene Hamiltonian reads as

$$\begin{aligned}H_{\mathrm{G}}(\delta\boldsymbol{k}) &= h^{\mathrm{gr}}_{\tau\boldsymbol{K}}(\delta\boldsymbol{k}) + H_{\mathrm{VZ}} + H_{\mathrm{R}}\\ &= \hbar v_F(\tau k_x\sigma_x + k_y\sigma_y) + \lambda_{\mathrm{VZ}}\,\tau s_z\\ &\quad + (\lambda_{\mathrm{R,tot}}/2)\,e^{-i\vartheta_{\mathrm{tot}}s_z/2}(\tau\sigma_x s_y - \sigma_y s_x)e^{i\vartheta_{\mathrm{tot}}s_z/2},\end{aligned} \tag{18}$$

using Eqs. (1) and (12) for the first two terms and Eq. (17) for H_{R}.

VII. DISCUSSION

In order to show explicitly how the twist angle θ between the layers affects the induced SOC in graphene, we need the band structure of the TMDC substrate and the weights $c_{b,x,y,z}(\tau\boldsymbol{k}'_1)$ for all backfolded points $\boldsymbol{k}'_1$ in the BZ along the path shown in Fig. 2. As a concrete example, we take monolayer MoS_2 (lattice constant $a_T = 3.15$ Å [28]) and we extract these values from the TB model of Ref. [50]. We have checked that the p orbital weights $c_{b,x,y,z}(\tau\boldsymbol{k}'_1)$ extracted from this TB model agree quite well with the corresponding results of Ref. [28] along high-symmetry directions in the Brillouin zone. We assume therefore that these weights can be reliably extracted for the relevant non-high-symmetry momentum space points shown in Fig. 2. Similarly, since the band structure calculated from this TB model agrees well with the DFT band structure, we assume that the spin-orbit splitting and the band-edge energy differences of the TMDC bands can be reliably extracted for all momentum space points of

interest. The *ab initio* calculations from Ref. [33] show the Dirac point very close to the conduction band of MoS_2, while experimental results reported in Ref. [35] indicate that the Dirac point should be found in the middle of the MoS_2 band gap. Because of these discrepancies, we treat the energy of the Dirac point of graphene within the band gap of the TMDC as a parameter in our theory. We parametrize this energy by a number $f_G \in [0, 1]$ whose value is a linear function of the position of the Dirac point in the TMDC band gap. When $f_G = 0$, the Dirac point is aligned with the TMDC valence band edge, while for $f_G = 1$ the Dirac point has the same energy as the TMDC conduction band edge.

According to Eq. (12), the strength of the induced valley Zeeman SOC has three main contributions from each band b: (i) it is proportional to the magnitude square of the tunneling strength $|t_b|^2$ and (ii) to the spin splitting $\Delta_{0,b}$, while (iii) it is inversely proportional to the energy difference $E_b^2 - \Delta_{0,b}^2$. In our numerical calculations of λ_{VZ}, shown in Figs. 3(c) and 3(d), we take into account two bands, the conduction ($b = c$) and the valence ($b = v$) bands (CB and VB). We plot $\Delta_{0,c}$ and $\Delta_{0,v}$ in Figs. 3(a) and 3(b) for the whole BZ of monolayer MoS_2 and in Fig. 3(e) along the path of the $\boldsymbol{k}_j'$ points. Again along this path, we report the values of $|t_c|^2$ and $|t_v|^2$ in Fig. 3(f).

First, we consider the case of the Dirac point close to the conduction band ($f_G \approx 1$) as reported by DFT calculations [33]. Using Eq. (12), the calculated λ_{VZ} is plotted in Fig. 3(c). One can see that starting from a small negative value at $\theta \gtrsim 0^\circ$, λ_{VZ} vanishes for $\theta \approx 10^\circ$ and then increases to 2 meV just before $\theta = 20^\circ$. Then, λ_{VZ} goes back to zero at $\theta = 30^\circ$ and the dependence is reflected with opposite sign between $\theta = 30^\circ$ and 60°. To understand these features, notice that Eqs. (10) and (12) suggest that when the Dirac point is very close to the CB (VB), the contribution from the VB (CB) to λ_{VZ} is suppressed by the large value of $E_v^2(\boldsymbol{k}_1')$ [$E_c^2(\boldsymbol{k}_1')$]. Hence, for $f_G \approx 1$, the behavior of λ_{VZ} over $\theta \in [0, \pi/3]$ is qualitatively well explained by the contribution of the CB and the VB can be neglected.

The reason for the vanishing λ_{VZ} for $\theta \approx 10^\circ$ and 30° is that also the TMDC CB spin splitting goes to zero and changes sign at these angles. The zero spin splitting at $\theta = 30^\circ$ appears because the backfolded points $\boldsymbol{k}_j'$ lie on the Γ-M line which by symmetry has no spin splitting [28]. In the case of $\theta \approx 10^\circ$, the backfolded points $\boldsymbol{k}_j'$ encounter a spin-splitting inversion of the TMDC conduction band [see Fig. 3(a)], i.e., the spin-split conduction bands cross along certain low-symmetry lines in the BZ. The peak around $\theta = 20^\circ$ is expected for multiple reasons. Close to $\theta = 20^\circ$ both spin splitting $\Delta_{0,c}(\boldsymbol{k}_1')$ and tunneling strength $t_c(\boldsymbol{K}^\theta)$ reach their largest absolute values [see green lines of Figs. 3(e) and 3(f)]. For $\Delta_{0,c}(\boldsymbol{k}_1')$ this happens because the backfolded points $\boldsymbol{k}_j'$ in the TMDC BZ get very close to the Q valley of the CB, in the middle of the Γ-K line, which has large spin splitting [see Fig. 3(a)] [28]. The tunneling strength peak instead comes from a larger local weight of the p_z orbitals [larger magnitude of orbital amplitudes $c_{cz}(\tau\boldsymbol{k}_1')$ in Eq. (5)]. Additionally, the energy distance between the Dirac point of graphene and the bottom of the Q point, which is a valley of the CB, is also smaller than for other $\boldsymbol{k}_1'$ points in the BZ. We have checked that the above

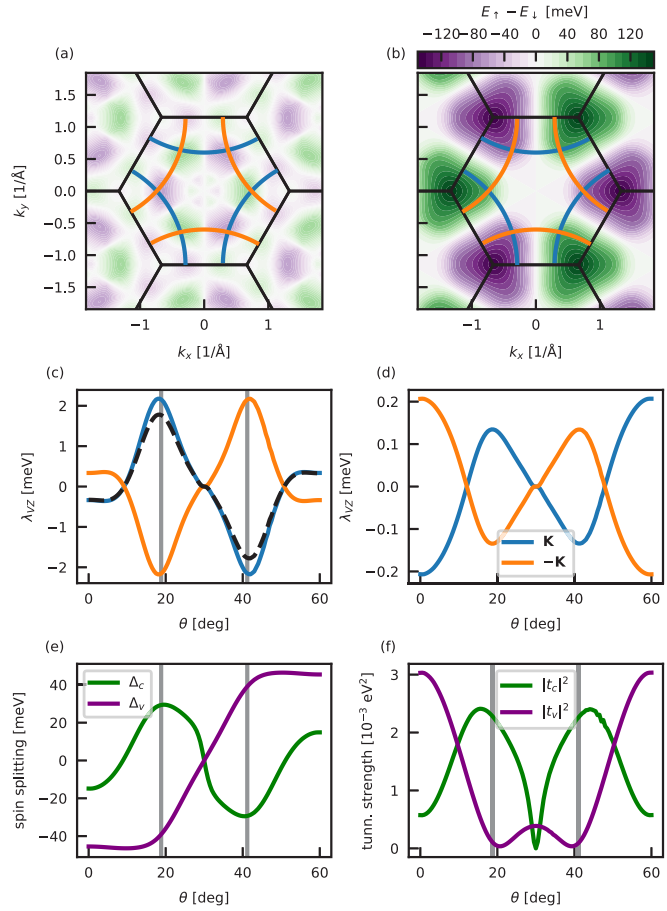

FIG. 3. (a), (b) Spin splitting in conduction (a) and valence band (b) of the TMDC. Blue (orange) arcs indicate the paths of the three backfolded vectors $\boldsymbol{k}_j'$ ($-\boldsymbol{k}_j'$) for Dirac point $\boldsymbol{K}$ ($-\boldsymbol{K}$). (c) Valley Zeeman spin-orbit strength induced in graphene when the Dirac point energy is close to the TMDC conduction band edge ($f_G = 1$). The blue (orange) line shows the result of second-order perturbation theory for Dirac point $\boldsymbol{K}$ ($-\boldsymbol{K}$), as derived in Eq. (12). The dashed black line is obtained from the exact diagonalization of the bilayer Hamiltonian (6) for $\boldsymbol{K}$. (d) Same as (c) but in the case when the Dirac point energy is in the middle of the TMDC band gap ($f_G = 0.55$) and with a larger TMDC band gap of $E_G = 2.0$ eV in order to reproduce the case of Ref. [35]. (e) Spin-orbit splitting in TMDC encountered by the backfolded vectors of $\boldsymbol{K}$ along the paths in (a) (green line) and (b) (purple line). (f) Tunneling strength squared for a tunneling process from graphene to the conduction (green line) or the valence band (purple line) of the TMDC. The gray vertical lines in (c), (e), and (f) highlight the angles where the backfolded vectors $\boldsymbol{k}_j'$ get as close as possible to the maximum of the spin splitting in the conduction band of the TMDC.

comments remain valid even if we add in the calculation the first band above the conduction band (CB + 1). Including this higher band does not change qualitatively the values of λ_{VZ}.

To confirm the behavior predicted by second-order perturbation theory, we have computed λ_{VZ} at $\delta\boldsymbol{k} = 0$ from exact diagonalization of the bilayer Hamiltonian in Eq. (6). Only the CB and the VB were taken into account in $h^{\mathrm{TMDC}}_{\tau\boldsymbol{k}_j'}$. The result is shown in Fig. 3(c) by a dashed black line. The agreement is very close except for the largest absolute values where the

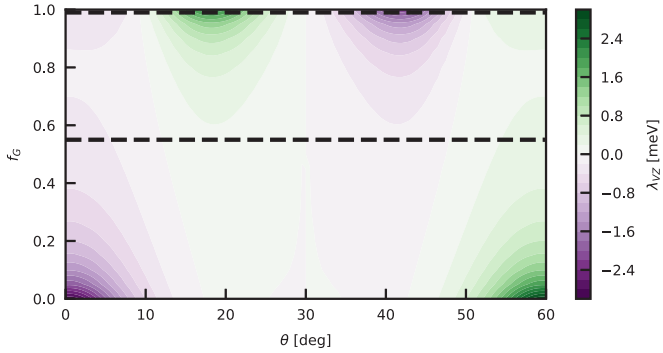

FIG. 4. Induced valley Zeeman SOC as a function of the twist angle θ and the parameter f_G that indicates how close the Dirac point lies to the conduction ($f_G = 1$) or to the valence band ($f_G = 0$). The dashed black lines indicate the two values of $f_G = 1$ and $f_G = 0.55$ used in Figs. 3(c) and 3(d), respectively.

second-order perturbation results deviates by around 10%. In these regions the Dirac points are quite near in energy to the CB of the TMDC and the small parameter $|t_b|/(E_b \pm \Delta_{0,b})$ increases up to 0.16. The numerical diagonalization of Eq. (6) also confirmed that in our model no spin-independent band gap is opened at the Dirac point.

It is known that DFT calculations (and TB models fitted to DFT calculations) underestimate the band gap of the TMDC. Indeed, the ARPES experiment of Ref. [35] reports a larger band gap of 2.0 eV. Moreover, according to Ref. [35], in graphene–TMDC bilayers, the Dirac point of graphene is found in the middle of the TMDC band gap ($f_G \approx 0.55$). For these reasons we have computed the induced valley Zeeman SOC in Eq. (12) for these alternative parameters (CB and VB dispersions were taken from the TB model as before). The results are plotted in Fig. 3(d). Here, the contribution from the VB is larger close to $\theta = 0^\circ$ and 60° [see purple lines in Figs. 3(e) and 3(f)] while it fades away around $\theta = 20^\circ$ and 40° where the CB contribution is more significant [see green lines in Figs. 3(e) and 3(f)]. Nevertheless, the values for λ_{VZ} predicted in Fig. 3(d) are one order of magnitude lower than those in Fig. 3(c) (Dirac point close to CB). They are indeed suppressed by the large distance of the Dirac point from both CB and VB. We show in Fig. 4 the value of λ_{VZ} computed from Eq. (12) for all values of f_G between 0 and 1. The dashed black lines indicate the two cuts at $f_G = 1$ [Fig. 3(c)] and $f_G = 0.55$ [Fig. 3(d)]. One can observe that close to the VB ($f_G \approx 0$) the induced valley Zeeman SOC is comparable to the values obtained for $f_G \approx 1$. However, for $f_G \approx 0$ the strongest induced SOC appear close to $\theta = 0^\circ$ and 60°. The contribution of the VB to the induced SOC can be important, e.g., for graphene-monolayer WSe_2 heterostructures, where DFT calculations [33] indicate that the Dirac point is closer to the VB edge.

In Fig. 5 we show the induced Rashba type SOC as a function of the twist angle θ between the layers. In these calculations we again considered MoS_2 as a concrete example. In Fig. 5(a) we have used $f_G = 1$, while in Fig. 5(b) we have set $f_G = 0.55$ and we have rigidly shifted the bands of the TMDC in order to reach a band gap of 2.0 eV. We have therefore reproduced the case of Ref. [35], as done for Fig. 3(d). The gray lines indicate the separate contributions

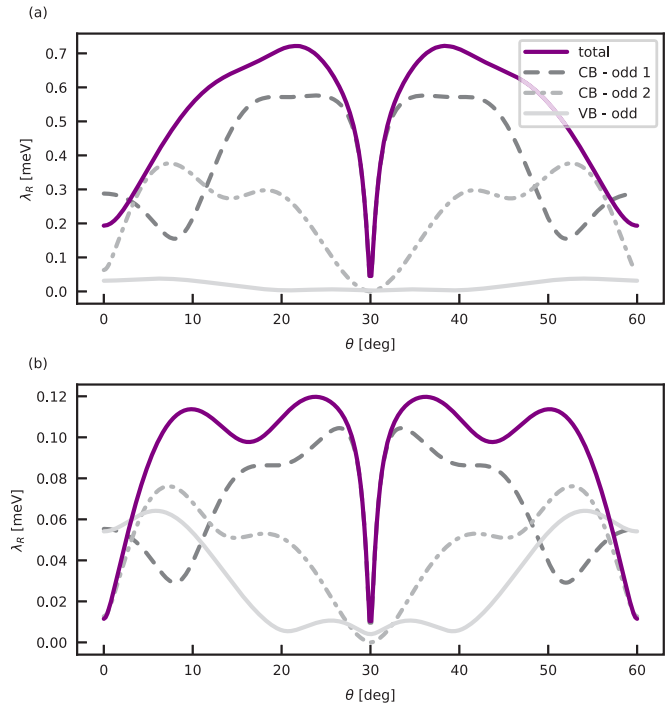

FIG. 5. Magnitude of the induced Rashba type SOC, λ_R, as a function of the twist angle θ for $f_G = 1$ (a) and $f_G = 0.55$ (b). In (b) we have also set the TMDC band gap to $E_G = 2.0$ eV in order to reproduce the case of Ref. [35]. The purple lines shows the total Rashba type SOC, the gray lines indicate separately the contribution related to two asymmetric bands above the conduction band and an asymmetric band below the valence band, respectively.

to Eq. (15) of three pairs of symmetric-antisymmetric bands. In particular, we consider the interaction of the symmetric CB with two asymmetric bands higher in energy and the interaction of the symmetric VB with one asymmetric band lower in energy. The purple lines represent the total sum of the three gray contributions taking into account the complex phases associated with them (see Appendix F for details of the calculation). One can see that the twist angle can considerably change the value of the SOC strength λ_R. For $f_G = 1$, a threefold increase of λ_R can be observed at $\theta \approx 20^\circ$ with respect to the $\theta = 0^\circ$ case. This is a somewhat smaller increase than in the case of λ_{VZ}, nevertheless, it shows that λ_R is tunable by the twist angle. The increase of λ_R close to 20° can partially be explained by the fact that one of the asymmetric bands, whose energy appears in the denominator of Eq. (15), is quite close to the conduction band in the vicinity of the Q point. Comparing Figs. 3(c) and 5(a) one can see that for $\theta \approx 0^\circ$ the values of λ_{VZ} and λ_R are comparable, while for $\theta \approx 20^\circ$ the valley Zeeman SOC dominates the Rashba type SOC. One can also see that λ_R drops to a small but nonzero value for $\theta = 30^\circ$. This can be qualitatively understood by looking at Fig. 3(f) which shows that the tunneling to the conduction band, which appears in the numerator of Eq. (16), has a sharp minimum for this angle. For the $f_G = 0.55$ case we notice that, similarly to the valley Zeeman SOC, the maximum value drops quite significantly. This is again a consequence of the large energy distance of the Dirac point from both the CB and the VB of the TMDC. However, the maximum value of

λ_R can still be found at a finite twist angle for $f_G = 0.55$, it does not shift to zero twist angle, as it does in the case of λ_{VZ}. In spite of this reduction of the strength of the induced SOC as a function of f_G, it may still be detected since a recent experiment has shown that SOC strengths of the order of $\sim$0.1 meV may be detected in graphene though resonance microwave measurements [57].

Finally, we note that Ref. [40] studied the same graphene-monolayer TMDC heterostructures using a TB model to describe both graphene and the monolayer TMDC and setting up a TB parametrization for the interlayer coupling. This approach, in principle, takes into account the coupling between all bands of the monolayer TMDC and graphene but also necessitates a number of new TB parameters to describe the interlayer coupling. For graphene-monolayer MoS_2 our results are, both for the induced valley Zeeman and the Rashba type SOC, qualitatively similar to Ref. [40], which indicates that our approach captures the most important ingredients contributing to the induced SOC. However, the vanishing and sign change of λ_{VZ} at $\theta \approx 10^\circ$ was not predicted in Ref. [40]. As explained above, we identified the band structure feature of the monolayer MoS_2 that gives rise to this behavior of λ_{VZ} and we believe that it is not an artifact of our approach. This feature should appear in graphene–TMDC bilayers for other semiconductor monolayer TMDC compounds, not only for MoS_2. Regarding the induced Rashba SOC, for $\theta = 0^\circ$ our result is in good qualitative agreement with Ref. [33], where λ_R was extracted from DFT calculations on commensurate graphene–TMDC supercells.

VIII. CONCLUSIONS AND OUTLOOK

In this paper we have presented the analytic twist-angle dependence of the induced spin-orbit coupling in graphene from the van der Waals interaction with monolayer TMDC. This fills the gap between experimental and theoretical works on twisted graphene–TMDC heterobilayers. While experiments most likely have a twist angle between the layers of the heterostructure, often unaccounted for in the analyses of the results and different from sample to sample, theory only considered zero or small twist angles. Here, we have shown that the induced SOC may vary significantly and even vanish as a function of the twist angle and of the position of the Dirac point in the TMDC band gap, therefore, the knowledge of both θ and f_G is important in order to compare experiments performed with different samples. The largest values of the induced valley Zeeman type SOC are $\sim$2 meV when the Dirac point of graphene is close to the conduction band of the TMDC. In comparison, the intrinsic spin-orbit coupling of isolated graphene is expected to be in the order of 20–40 μeV [8,57]. This indicates that, by juxtaposing monolayer TMDCs and by engineering the twist angle between the two layers, the induced SOC in graphene can be two orders of magnitude larger than the intrinsic one. We also identified a microscopic mechanism that gives rise to an induced Rashba type SOC and we have found that it can also be significantly enhanced as a function of the twist angle.

The use of a band-to-band tunneling picture was fundamental to reach our results. This framework simplifies the study of heterobilayers where the band structure of the individual constituent layers is well known and understood. Similarly to Ref. [40], it can also be used if the lattice constants of the individual layers are incommensurate. Moreover, as the complexity of the material increases and the number of orbitals involved in its valence and conduction bands becomes large, an orbital-to-orbital tunneling picture to describe interlayer tunneling would require a tight-binding model with many parameters. In graphene–TMDC heterostructures, by using the nearest chalcogen layer approximation and the Fourier transform of the Slater-Koster matrix elements, the interlayer tunneling parametrization was reduced to just two overlap integrals. The bands of the isolated layers can be approximated by $k \cdot p$ theory which helped to obtain the induced SOC by applying quasidegenerate perturbation theory. Using this approach we were able to separate the contribution from the different bands and analyze the behavior of the induced valley Zeeman and Rashba type SOC as a function of the interlayer twist angle. Our approach makes the role of the intrinsic properties of the substrate more apparent and, therefore, it might be used to screen potential substrate materials for desired induced SOC properties in van der Waals heterostructures.

We assumed perfectly ballistic layers in our work. An interesting extension would be to study the induced SOC in the presence of disorder effects. This may affect the interpretation of WAL measurements, as the interplay between spin, valley, and disorder physics yields a rich behavior of the quantum correction to the conductivity [58]. Another important effect might be the presence of graphene domains with different twist angles. According to Fig. 3(c), if the average twist angle is small, the induced valley Zeeman SOC can be positive in some domains and negative in others. The effects of such nonuniform induced SOC on, e.g., the spin-transport properties of the sample would require further studies.

ACKNOWLEDGMENTS

We acknowledge funding from the Deutsche Forschungsgemeinschaft (DFG) through Grant No. SFB767, from CAP Konstanz and from FlagERA through iSpinText. P.R. and A.K. were supported by NKFIH within the Quantum Technology National Excellence Program (Project No. 2017-1.2.1-NKP-2017-00001) and by Hungarian Scientific Research Fund, OTKA Grant No. NN 127903 (Topograph FlagERA project). P.R. also acknowledges the funding from OTKA Grants No. PD123927 and No. K123894. We would like to thank A. Pearce for technical assistance with Fig. 1 and V. Shkolnikov for helpful discussions.

APPENDIX A: DEFINITIONS OF LATTICE VECTORS

Graphene and monolayer TMDCs share the same 2D hexagonal structure, but with different lattice constants. As before, primed quantities are related to the TMDC. The primitive vectors for the hexagonal lattice are $\boldsymbol{a}_{1,2} = a(\pm 1/2, \sqrt{3}/2)$ with lattice constant $a = a_G$ ($a = a_T$) for graphene (TMDC). The B sublattice is shifted by $\boldsymbol{\delta} = a/\sqrt{3}(0, 1)$. The primitive reciprocal lattice vectors $\boldsymbol{b}_{1,2}$ follow the relation $\boldsymbol{a}_i \cdot \boldsymbol{b}_j = 2\pi\delta_{ij}$, where δ_{ij} is the Kronecker delta, and are explicitly given by $\boldsymbol{b}_{1,2} =$

$4\pi/a\sqrt{3}(\pm\sqrt{3}/2, 1/2)$. In the heterobilayer studied in this paper, graphene is on top of the TMDC layer, separated from the topmost TMDC chalcogen layer by $d_\perp$ (see Fig. 1). The positions of the atoms in the unit cell are given by $\boldsymbol{\tau}_X$ for graphene and by $\boldsymbol{\tau}_{X'}$ for the TMDC, with $X = A, B$ and $X' = A', B'_1, B'_2$, where B'_1 (B'_2) indicates the upper (lower) chalcogen atom site. We fix the origin of our coordinate system above a metal atom in the TMDC, but in the same plane as the upper chalcogen layer,

$$\boldsymbol{\tau}_A = d_\perp \hat{\boldsymbol{e}}_z, \quad \boldsymbol{\tau}_B = \boldsymbol{\delta} + d_\perp \hat{\boldsymbol{e}}_z,$$
$$\boldsymbol{\tau}_{A'} = -\frac{d_{X\text{-}X}}{2}\hat{\boldsymbol{e}}_z, \quad \boldsymbol{\tau}_{B'_1} = \boldsymbol{\delta}', \quad \boldsymbol{\tau}_{B'_2} = \boldsymbol{\delta}' - d_{X\text{-}X}\hat{\boldsymbol{e}}_z, \tag{A1}$$

with $d_{X\text{-}X}$ the TMDC chalcogen-chalcogen distance.

APPENDIX B: SLATER-KOSTER TUNNELING COEFFICIENTS AND THEIR FOURIER TRANSFORM

We are interested in the tunneling between the p_z orbitals of the carbon atoms in graphene and the p orbitals of the closest TMDC chalcogen layer. Using the two-center approximation, the real-space tunneling matrix elements $T_{XX'}(\boldsymbol{R})$ can be written in terms of Slater-Koster parameters [49]

$$T_{p_z,p_z}(\boldsymbol{R}) = n_z^2 V_{pp\sigma}(R) + \left(1 - n_z^2\right) V_{pp\pi}(R), \tag{B1a}$$
$$T_{p_z,p_{x\,(y)}}(\boldsymbol{R}) = n_{x\,(y)} n_z [V_{pp\sigma}(R) - V_{pp\pi}(R)], \tag{B1b}$$

with $R = |\boldsymbol{R}|$ and $(n_x, n_y, n_z) = \boldsymbol{R}/R$. Since $X = A, B$ refers always to the p_z orbitals of the carbon atoms in graphene, there is no real dependence on X and we omit it in the following, $T_{XX'} = T_{X'}$.

In cylindrical coordinates (r, φ, z) we have $\boldsymbol{r} = r\cos\varphi\,\hat{\boldsymbol{e}}_x + r\sin\varphi\,\hat{\boldsymbol{e}}_y$, $\boldsymbol{R} = \boldsymbol{r} + z\hat{\boldsymbol{e}}_z$, $R = \sqrt{r^2 + z^2}$, and

$$n_x = \frac{r\cos\varphi}{\sqrt{r^2+z^2}}, \quad n_y = \frac{r\sin\varphi}{\sqrt{r^2+z^2}}, \quad n_z = \frac{z}{\sqrt{r^2+z^2}}.$$

We can separate the radial part from the angular part in Eqs. (B1),

$$T_{p_z}(r, \varphi, z) = f_z(r, z), \tag{B2a}$$
$$T_{p_x}(r, \varphi, z) = \cos\varphi\, f_x(r, z), \tag{B2b}$$
$$T_{p_y}(r, \varphi, z) = \sin\varphi\, f_x(r, z), \tag{B2c}$$

where

$$f_z(r, z) = \frac{1}{R^2}[z^2 V_{pp\sigma}(R) + r^2 V_{pp\pi}(R)],$$
$$f_x(r, z) = f_y(r, z) = \frac{rz}{R^2}[V_{pp\sigma}(R) - V_{pp\pi}(R)]. \tag{B3}$$

In Eqs. (B2), we refer to the φ-dependent parts as $a_{X'}(\varphi)$, with $a_z(\varphi) = 1$, $a_x(\varphi) = \cos\varphi$, and $a_y(\varphi) = \sin\varphi$. Hence, we can write $T_{X'}(r, \varphi, z) = a_{X'}(\varphi) f_{X'}(r, z)$. Then, we take the Fourier transform of Eqs. (B1) [47]:

$$t_{X'}(\boldsymbol{q}) = \frac{1}{\sqrt{SS'}}\int T_{X'}(\boldsymbol{r} + z\hat{\boldsymbol{e}}_z) e^{-i\boldsymbol{q}\cdot\boldsymbol{r}} d^2 r$$
$$= \frac{1}{\sqrt{SS'}}\int_0^\infty dr\, r f_{X'}(r, z) \times \int_{-\pi}^{\pi} d\varphi\, a_{X'}(\varphi) e^{-iqr\cos(\varphi-\varphi_q)}, \tag{B4}$$

where $\boldsymbol{q} = (q\cos\varphi_q, q\sin\varphi_q)$ and S (S') is the unit-cell size of graphene (TMDC). The integral over the angle can be solved using the Jacobi-Anger expansion [59,60]

$$\int_{-\pi}^{\pi} d\varphi\, e^{-iqr\cos(\varphi-\varphi_q)} = 2\pi J_0(qr), \tag{B5a}$$
$$\int_{-\pi}^{\pi} d\varphi\, \cos\varphi\, e^{-iqr\cos(\varphi-\varphi_q)} = -2\pi i J_1(qr)\cos\varphi_q, \tag{B5b}$$
$$\int_{-\pi}^{\pi} d\varphi\, \sin\varphi\, e^{-iqr\cos(\varphi-\varphi_q)} = -2\pi i J_1(qr)\sin\varphi_q, \tag{B5c}$$

where $J_m(x)$ is the mth-order Bessel function of the first kind. We see that the angular dependence of the tunneling matrix elements is preserved when switching from real space to momentum space. One may write

$$t_{X'}(q, \varphi_q, z) = (-i)^m a_{X'}(\varphi_q) P_{X'}(q, z), \tag{B6}$$

where $P_{X'}(q, z)$ is real and equal to the integral of the radial part

$$P_{X'}(q, z) = \frac{2\pi}{\sqrt{SS'}}\int_0^\infty dr\, r f_{X'}(r, z) J_m(qr), \tag{B7}$$

with $m = 0$ for $X' = p_z$, while $m = 1$ for $X' = p_x, p_y$.

We define the tunneling strength from graphene to a band of the TMDC as

$$t_b(\boldsymbol{k}' + \boldsymbol{G}') = \sum_{X'} c_{bX'}(\boldsymbol{k}') t_{X'}(\boldsymbol{k}' + \boldsymbol{G}'), \tag{B8}$$

where $\boldsymbol{k}'$ is a vector inside the first TMDC BZ, $\boldsymbol{G}'$ is a reciprocal lattice vector of the TMDC, and $c_{bX'}(\boldsymbol{k}')$ is the amplitude of orbital X' in band b, the index X' runs over the three p orbitals of the chalcogen atom. We derive here the form of Eq. (B8) for the points $\tau(\boldsymbol{k}'_j + \boldsymbol{G}'_j)$ of Eq. (4), with $\boldsymbol{G}'_1 = \boldsymbol{b}'_1$, $\boldsymbol{G}'_2 = \boldsymbol{b}'_2$, and $\boldsymbol{G}'_3 = -\boldsymbol{b}'_1 - \boldsymbol{b}'_2$. Using the quasimomentum conservation we have $\tau(\boldsymbol{k}'_j + \boldsymbol{G}'_j) = \tau(\boldsymbol{K}^\theta + \boldsymbol{G}^\theta_j) =: \tau\boldsymbol{K}^\theta_j$, with $\boldsymbol{G}_1 = 0$, $\boldsymbol{G}_2 = \boldsymbol{b}_2$, and $\boldsymbol{G}_3 = -\boldsymbol{b}_1$ (see Fig. 2). We remark here that all vectors $\tau\boldsymbol{K}^\theta_j$ have the same magnitude K. Renaming the in-plane integral as $-P_x(K, z_1) \equiv -P_y(K, z_1) \equiv t_\parallel$ and the out-of-plane integral as $P_z(K, z_1) \equiv t_\perp$, with $z_1 = d_\perp$, we have then

$$t_b(\tau\boldsymbol{K}^\theta_j) = i\left[c_{bx}(\tau\boldsymbol{k}'_j)\cos\varphi_{\tau\boldsymbol{K}^\theta_j} + c_{by}(\tau\boldsymbol{k}'_j)\sin\varphi_{\tau\boldsymbol{K}^\theta_j}\right] t_\parallel + c_{bz}(\tau\boldsymbol{k}'_j)\, t_\perp, \tag{B9}$$

where $\varphi_{\tau\boldsymbol{K}^\theta_j}$ is the polar angle of $\tau\boldsymbol{K}^\theta_j$. One may write $\varphi_{\tau\boldsymbol{K}^\theta_j} = \varphi_{\tau\boldsymbol{K}_j} + \theta$ with $\varphi_{\boldsymbol{K}_1} = \varphi_{\boldsymbol{K}} = 0$, $\varphi_{\boldsymbol{K}_2} = 2\pi/3$, and $\varphi_{\boldsymbol{K}_3} = -2\pi/3$, while $\varphi_{-\boldsymbol{K}_j} = \varphi_{\boldsymbol{K}_j} + \pi$. We treat $t_\parallel$ and $t_\perp$ as two real parameters to be determined from experiments, *ab initio* calculations, or tight-binding models.

APPENDIX C: SYMMETRY OF ORBITAL AMPLITUDES IN A TMDC BAND

To define the tunneling strength in Eq. (B8), we have expanded the state of an electron in band b of the TMDC as a linear combination of single-orbital Bloch states

$$|b, \boldsymbol{k}'\rangle = \sum_{X'} c_{bX'}(\boldsymbol{k}')\,|X', \boldsymbol{k}'\rangle\,. \tag{C1}$$

The properties of the coefficients $c_{bX'}(\boldsymbol{k}')$ therefore play an important role in the form of the bilayer Hamiltonian (6). These coefficients are constrained by the TMDC lattice symmetry and the coordinate transformations of the orbitals and of the Bloch states. We prove a useful relation focusing on $c_{b,x}(\boldsymbol{k}')$ and $c_{b,y}(\boldsymbol{k}')$, the coefficients of orbitals p_x and p_y, respectively. For the sake of clarity we indicate $|X', \boldsymbol{k}'\rangle \equiv |\psi_{X'}, \boldsymbol{k}'\rangle$, where we made the orbital wave function $\psi_{X'}$ explicit, $\langle \boldsymbol{r}|\psi_{X'}\rangle = \psi_{X'}(\boldsymbol{r})$, with $\boldsymbol{r} = (x, y, z)^T$.

Consider two wave vectors $\boldsymbol{k}'$ and $R(\alpha)\boldsymbol{k}'$ where $R(\alpha)$ is a rotation of the point group of the TMDC crystal, i.e., $\alpha = \pm 2\pi/3$. Following Ref. [61], we know that

$$|b, R(\alpha)\boldsymbol{k}'\rangle = R(\alpha)\,|b, \boldsymbol{k}'\rangle = \sum_{X'} c_{bX'}(\boldsymbol{k}')R(\alpha)\,|\psi_{X'}, \boldsymbol{k}'\rangle\,. \tag{C2}$$

For a single-orbital Bloch state $|\psi_{X'}, \boldsymbol{k}'\rangle$, the transformation under rotation results in a rotation of the orbital wave function

$$\begin{aligned}\langle \boldsymbol{r}|R(\alpha)|\psi_{X'}, \boldsymbol{k}'\rangle &= \langle R(-\alpha)\boldsymbol{r}|\psi_{X'}, \boldsymbol{k}'\rangle = \frac{1}{\sqrt{N'}}\sum_{\boldsymbol{R}_{X'}} e^{i\boldsymbol{k}'\cdot\boldsymbol{R}_{X'}}\psi_{X'}(R(-\alpha)\boldsymbol{r} - \boldsymbol{R}_{X'})\\ &= \frac{1}{\sqrt{N'}}\sum_{\boldsymbol{R}_{X'}} e^{i\boldsymbol{k}'\cdot\boldsymbol{R}_{X'}}\psi_{X'}(R(-\alpha)[\boldsymbol{r} - R(\alpha)\boldsymbol{R}_{X'}]) = \frac{1}{\sqrt{N'}}\sum_{\widetilde{\boldsymbol{R}}_{X'}} e^{i\boldsymbol{k}'\cdot R(-\alpha)\widetilde{\boldsymbol{R}}_{X'}}[R(\alpha)\psi_{X'}](\boldsymbol{r} - \widetilde{\boldsymbol{R}}_{X'})\\ &= \frac{1}{\sqrt{N'}}\sum_{\widetilde{\boldsymbol{R}}_{X'}} e^{iR(\alpha)\boldsymbol{k}'\cdot\widetilde{\boldsymbol{R}}_{X'}}[R(\alpha)\psi_{X'}](\boldsymbol{r} - \widetilde{\boldsymbol{R}}_{X'}) = \langle \boldsymbol{r}|R(\alpha)\psi_{X'}, R(\alpha)\boldsymbol{k}'\rangle\,,\end{aligned} \tag{C3}$$

therefore,

$$R(\alpha)\,|\psi_{X'}, \boldsymbol{k}'\rangle = |R(\alpha)\psi_{X'}, R(\alpha)\boldsymbol{k}'\rangle\,. \tag{C4}$$

Due to the linear dependence of $p_x(\boldsymbol{r})$ and $p_y(\boldsymbol{r})$ on x and y, respectively, we have the following transformations for $\psi_{X'} = p_x, p_y$:

$$\begin{aligned}(R(\alpha)p_x)(\boldsymbol{r}) &= p_x(R(-\alpha)\boldsymbol{r}) = \cos\alpha\; p_x(\boldsymbol{r}) + \sin\alpha\; p_y(\boldsymbol{r}),\\ (R(\alpha)p_y)(\boldsymbol{r}) &= p_y(R(-\alpha)\boldsymbol{r}) = -\sin\alpha\; p_x(\boldsymbol{r}) + \cos\alpha\; p_y(\boldsymbol{r}),\end{aligned} \tag{C5}$$

which is reflected then in the Bloch states

$$\begin{aligned}|R(\alpha)p_x, \boldsymbol{k}'\rangle &= \cos\alpha\;|p_x, \boldsymbol{k}'\rangle + \sin\alpha\;|p_y, \boldsymbol{k}'\rangle\,,\\ |R(\alpha)p_y, \boldsymbol{k}'\rangle &= -\sin\alpha\;|p_x, \boldsymbol{k}'\rangle + \cos\alpha\;|p_y, \boldsymbol{k}'\rangle\,.\end{aligned} \tag{C6}$$

Finally, multiplying the left- and the right-hand sides of Eq. (C2) by $\langle\psi_{\widetilde{X}'}, R(\alpha)\boldsymbol{k}'|$ and using the orthogonality between p_x and p_y orbitals, we obtain

$$\begin{aligned}c_{b,x}(R(\alpha)\boldsymbol{k}') &= \cos\alpha\; c_{b,x}(\boldsymbol{k}') - \sin\alpha\; c_{b,y}(\boldsymbol{k}'),\\ c_{b,y}(R(\alpha)\boldsymbol{k}') &= \sin\alpha\; c_{b,x}(\boldsymbol{k}') + \cos\alpha\; c_{b,y}(\boldsymbol{k}'),\end{aligned} \tag{C7}$$

which can be written in short form as

$$\boldsymbol{c}_b(R(\alpha)\boldsymbol{k}') = R(\alpha)\boldsymbol{c}_b(\boldsymbol{k}'), \tag{C8}$$

with $\boldsymbol{c}_b(\boldsymbol{k}') = (c_{b,x}(\boldsymbol{k}'), c_{b,y}(\boldsymbol{k}'))^T$.

We need Eq. (C8) to prove that the band tunneling strength in Eq. (B9) has the same value for all the three backfolded vectors $\tau\boldsymbol{k}'_j$ in Eq. (4). Equation (B9) can be rewritten as

$$t_b\big(\tau\boldsymbol{K}^\theta_j\big) = \boldsymbol{c}_b(\tau\boldsymbol{k}'_j)\cdot R\big(\varphi_{\tau\boldsymbol{K}^\theta_j}\big)\boldsymbol{t}, \tag{C9}$$

where $\boldsymbol{t} = (it_\parallel, 0, t_\perp)$. Here, we have included the p_z coefficient $c_{b,z}(\tau\boldsymbol{k}'_j)$ in the vector $\boldsymbol{c}_b(\tau\boldsymbol{k}'_j)$ and the rotation operator $R(\varphi_{\tau\boldsymbol{K}^\theta_j})$ is a 3×3 matrix rotating only the first two components of $\boldsymbol{t}$ while leaving the third one unchanged. We show that $t_b(\boldsymbol{K}^\theta_2) = t_b(\boldsymbol{K}^\theta_1)$ and one can obtain similar results for $\boldsymbol{K}^\theta_3$ and for the opposite Dirac point ($\tau = -$). We remark that $\varphi_{\boldsymbol{K}^\theta_2} = \varphi_{\boldsymbol{K}^\theta_1} + 2\pi/3$. Then,

$$\begin{aligned}t_b\big(\boldsymbol{K}^\theta_2\big) &= \boldsymbol{c}_b(\boldsymbol{k}'_2)\cdot R\big(\varphi_{\boldsymbol{K}^\theta_2}\big)\boldsymbol{t}\\ &= \boldsymbol{c}_b(R(2\pi/3)\boldsymbol{k}'_1)\cdot R\big(\varphi_{\boldsymbol{K}^\theta_1} + 2\pi/3\big)\boldsymbol{t}\\ &= \boldsymbol{c}_b(\boldsymbol{k}'_1)\cdot R\big(\varphi_{\boldsymbol{K}^\theta_1}\big)\boldsymbol{t} = t_b\big(\boldsymbol{K}^\theta_1\big),\end{aligned} \tag{C10}$$

where we have used Eq. (C8). It follows that we need to compute the band tunneling strength only for $\tau\boldsymbol{K}^\theta_1 = \tau\boldsymbol{K}^\theta$. Since $\varphi_{\boldsymbol{K}^\theta} = \theta$ and $\varphi_{-\boldsymbol{K}^\theta} = \theta + \pi$, we can write Eq. (B9) as

$$\begin{aligned}t_b(\tau\boldsymbol{K}^\theta) = i\tau[&c_{bx}(\tau\boldsymbol{k}'_1)\cos\theta + c_{by}(\tau\boldsymbol{k}'_1)\sin\theta]\;t_\parallel\\ &+ c_{bz}(\tau\boldsymbol{k}'_1)\;t_\perp.\end{aligned} \tag{C11}$$

APPENDIX D: SECOND-ORDER SCHRIEFFER-WOLFF TRANSFORMATION

Here, we derive Eqs. (11) and (13). Following Ref. [53], the second-order Schrieffer-Wolff matrix elements of the bilayer Hamiltonian (6) are given by

$$\delta H^{\mathrm{gr},\tau}_{Xs,X's'} = \sum_{j,b,s''}\frac{\big(T_{\tau\boldsymbol{k}'_j}\big)_{Xs,bs''}\big(T^\dagger_{\tau\boldsymbol{k}'_j}\big)_{bs'',X's'}}{E^{\mathrm{gr}}_D - E^{\mathrm{TMDC}}_{bs''}(\tau\boldsymbol{k}'_j + \delta\boldsymbol{k})}, \tag{D1}$$

where $X, X' = A, B$ refer to the graphene sublattices, $s, s', s'' = \uparrow, \downarrow$ are spin indices, $j = 1, 2, 3$, and b is the band index. Moreover, E^{gr}_D is the energy of the Dirac point that we fix, without loss of generality, to $E^{\mathrm{gr}}_D = 0$, while $E^{\mathrm{TMDC}}_{bs}(\tau\boldsymbol{k}'_j + \delta\boldsymbol{k})$ is the energy of the TMDC band b, spin index s, at the BZ point $\tau\boldsymbol{k}'_j + \delta\boldsymbol{k}$. Using the spin-preserving property of Eq. (9), one has that $\delta H^{\mathrm{gr},\tau}_{Xs,X's'} = 0$ for $s \neq s'$ and the elements for equal spin are given by Eq. (10). In the following, we treat diagonal and off-diagonal elements separately.

Considering first the diagonal elements ($X' = X$), we expand the numerator using Eq. (9),

$$\delta H^{\mathrm{gr},\tau}_{Xs,Xs} = -\sum_{j,b} \frac{|t_b(\tau \boldsymbol{K}^\theta)|^2}{E^{\mathrm{TMDC}}_{bs}(\tau \boldsymbol{k}'_j + \delta\boldsymbol{k})}. \tag{D2}$$

Then, we continue by expanding the $\delta\boldsymbol{k}$ dependence of $E^{\mathrm{TMDC}}_{bs}(\tau\boldsymbol{k}'_j + \delta\boldsymbol{k})$ using $k\cdot p$ theory [28]. For a general $\boldsymbol{k}'_1$ point in the TMDC BZ,

$$E^{\mathrm{TMDC}}_{bs}(\tau\boldsymbol{k}'_1 + \delta\boldsymbol{k}) = E_b(\boldsymbol{k}'_1) + s\tau\Delta_{0,b}(\boldsymbol{k}'_1) + [w_{x,b}(\boldsymbol{k}'_1) + s\tau\Delta_{1x,b}(\boldsymbol{k}'_1)]\tau\delta\boldsymbol{k}_x + [w_{y,b}(\boldsymbol{k}'_1) + s\tau\Delta_{1y,b}(\boldsymbol{k}'_1)]\tau\delta\boldsymbol{k}_y + \frac{\hbar^2\delta\boldsymbol{k}_x^2}{2m_x^{\tau,s}(\boldsymbol{k}'_1)} + \frac{\hbar^2\delta\boldsymbol{k}_y^2}{2m_y^{\tau,s}(\boldsymbol{k}'_1)} + \frac{\hbar^2\delta\boldsymbol{k}_x\delta\boldsymbol{k}_y}{2m_{xy}^{\tau,s}(\boldsymbol{k}'_1)} + \mathcal{O}(\delta\boldsymbol{k}^3), \tag{D3}$$

where E_b, $\Delta_{0,b}$, $w_{x,b}$, $w_{y,b}$, $\Delta_{1x,b}$, $\Delta_{1y,b}$, $m_x^{\tau,s}$, $m_y^{\tau,s}$, $m_{xy}^{\tau,s}$ are material parameters for band b locally dependent on the BZ point. They can be extracted from experiments, *ab initio* calculations, or tight-binding models. In particular, E_b is the energy of band b (ignoring SOC) with respect to the Dirac point of graphene, $\Delta_{0,b}$ is the local spin splitting, $w_{x,b}$, $w_{y,b}$, $\Delta_{1x,b}$, $\Delta_{1y,b}$ describe the local slope of the band, and $m_x^{\tau,s}$, $m_y^{\tau,s}$, $m_{xy}^{\tau,s}$ are the effective masses of the quadratic dispersion. The $k\cdot p$ expansion close to $\boldsymbol{k}'_{2,3}$ is obtained from $E^{\mathrm{TMDC}}_{bs}(\tau\boldsymbol{k}'_1 + \delta\boldsymbol{k})$ by rotating $\delta\boldsymbol{k}$ according to Eq. (8). One may write

$$E^{\mathrm{TMDC}}_{bs}(\tau\boldsymbol{k}'_j + \delta\boldsymbol{k}) = E^{\mathrm{TMDC}}_{bs}(\tau\boldsymbol{k}'_1 + \delta\boldsymbol{k}^{-\varphi_j}), \tag{D4}$$

with $\varphi_j = 0, 2\pi/3, -2\pi/3$ for $j = 1, 2, 3$. We expand the denominator of Eq. (D2) with Eqs. (D3) and (D4) and we retain up to linear terms in $\delta\boldsymbol{k}$,

$$\frac{1}{E^{\mathrm{TMDC}}_{bs}(\tau\boldsymbol{k}'_j + \delta\boldsymbol{k})} \approx \frac{1}{E_{bs\tau}(\boldsymbol{k}'_1)} - \frac{\boldsymbol{w}_{bs\tau}(\boldsymbol{k}'_1)\cdot\tau\delta\boldsymbol{k}^{-\varphi_j}}{E_{bs\tau}(\boldsymbol{k}'_1)^2}, \tag{D5}$$

where $E_{bs\tau}(\boldsymbol{k}'_1) = E_b(\boldsymbol{k}'_1) + s\tau\Delta_{0,b}(\boldsymbol{k}'_1)$ and $\boldsymbol{w}_{bs\tau}(\boldsymbol{k}'_1) = (w_{x,b}(\boldsymbol{k}'_1) + s\tau\Delta_{1x,b}(\boldsymbol{k}'_1), w_{y,b}(\boldsymbol{k}'_1) + s\tau\Delta_{1y,b}(\boldsymbol{k}'_1))^T$. This holds under the condition that $|\boldsymbol{w}_{bs\tau}(\boldsymbol{k}'_1)\cdot\delta\boldsymbol{k}^{-\varphi_j}| \ll |E_{bs\tau}(\boldsymbol{k}'_1)|$ and terms containing higher powers of $\delta\boldsymbol{k}$ are therefore negligible. Substituting Eq. (D5) in (D2) we have

$$\delta H^{\mathrm{gr},\tau}_{Xs,Xs} = A_{bs\tau} + B_{bs\tau,x}\tau\delta\boldsymbol{k}_x + B_{bs\tau,y}\tau\delta\boldsymbol{k}_y, \tag{D6}$$

which is a sum of a $\delta\boldsymbol{k}$-independent part

$$A_{bs\tau} = -3\sum_b \frac{|t_b(\tau\boldsymbol{K}^\theta)|^2}{E_{bs\tau}(\boldsymbol{k}'_1)}, \tag{D7}$$

and a $\delta\boldsymbol{k}$-dependent part whose coefficients are given by

$$B_{bs\tau,\xi} = \sum_b \frac{|t_b(\tau\boldsymbol{K}^\theta)|^2}{E_{bs\tau}(\boldsymbol{k}'_1)^2}\sum_j (R(\varphi_j)\boldsymbol{w}_{bs\tau}(\boldsymbol{k}'_1))_\xi \tag{D8}$$

for $\xi = x, y$. The factor of 3 in Eq. (D7) comes from the sum over index j. On the other hand, one can see that the sum over j in Eq. (D8) gives zero because it is the sum of three vectors with same magnitude that are rotated by $\pm 2\pi/3$. Therefore, $\delta H^{\mathrm{gr},\tau}_{Xs,Xs} = A_{bs\tau}$ as reported in Eq. (11).

Now, we focus on the off-diagonal elements ($X' \neq X$) of Eq. (D1) and we expand again the numerator using Eq. (9). Only two independent off-diagonal elements are nonzero, namely,

$$\delta H^{\mathrm{gr},\tau}_{As,Bs} = -\sum_{j,b} \frac{|t_b(\tau\boldsymbol{K}^\theta)|^2 e^{-i\tau\phi_j}}{E^{\mathrm{TMDC}}_{bs}(\tau\boldsymbol{k}'_j + \delta\boldsymbol{k})} \tag{D9}$$

for $s = \uparrow, \downarrow$. The other elements are given by $\delta H^{\mathrm{gr},\tau}_{Bs,As} = (\delta H^{\mathrm{gr},\tau}_{As,Bs})^*$. Equation (D9) is similar to Eq. (D2), but it has additional phase factors $e^{-i\tau\phi_j}$. Expanding the denominator as before, we arrive to the equivalent of Eq. (D6),

$$\delta H^{\mathrm{gr},\tau}_{As,Bs} = A^{\mathrm{off}}_{bs\tau} + B^{\mathrm{off}}_{bs\tau,x}\tau\delta\boldsymbol{k}_x + B^{\mathrm{off}}_{bs\tau,y}\tau\delta\boldsymbol{k}_y, \tag{D10}$$

where

$$A^{\mathrm{off}}_{bs\tau} = -\sum_{j,b} \frac{|t_b(\tau\boldsymbol{K}^\theta)|^2 e^{-i\tau\phi_j}}{E_{bs\tau}(\boldsymbol{k}'_1)} \tag{D11}$$

and

$$B^{\mathrm{off}}_{bs\tau,\xi} = \sum_b \frac{|t_b(\tau\boldsymbol{K}^\theta)|^2}{E_{bs\tau}(\boldsymbol{k}'_1)^2}\sum_j e^{-i\tau\phi_j}(R(\varphi_j)\boldsymbol{w}_{bs\tau}(\boldsymbol{k}'_1))_\xi. \tag{D12}$$

The two sets of angles ϕ_j and φ_j have the same values ($0, 2\pi/3, -2\pi/3$ for $j = 1, 2, 3$), but different origins. The angles ϕ_j come from the tunneling matrix elements in Eq. (9) and are connected to the C_3 symmetry of graphene. Instead, the angles φ_j are connected to the C_3 symmetry of the TMDC crystal and they come from Eq. (D4). The sum over j in Eq. (D11) gives zero because $e^{-i\tau\phi_j}$ are the complex cube roots of the unity and sum to zero. In order to carry out the sum over j in Eq. (D12) we compute

$$B^{\mathrm{off}}_{bs\tau,x} \pm iB^{\mathrm{off}}_{bs\tau,y} = \sum_b \frac{|t_b(\tau\boldsymbol{K}^\theta)|^2}{E_{bs\tau}(\boldsymbol{k}'_1)^2} w_{bs\tau,\pm}(\boldsymbol{k}'_1)\sum_j e^{-i\tau\phi_j \pm i\varphi_j}, \tag{D13}$$

with $w_{bs\tau,\pm}(\boldsymbol{k}'_1) = w_{x,b}(\boldsymbol{k}'_1) + s\tau\Delta_{1x,b}(\boldsymbol{k}'_1) \pm i(w_{y,b}(\boldsymbol{k}'_1) + s\tau\Delta_{1y,b}(\boldsymbol{k}'_1))$. Looking at Eq. (D13), the sum $\sum_j e^{-i\tau\phi_j + i\varphi_j}$ is equal to 3 for $\tau = +$ and it is equal to 0 for $\tau = -$. On the other hand, $\sum_j e^{-i\tau\phi_j - i\varphi_j} = 0$ for $\tau = +$ and is equal to 3 for $\tau = -$. We conclude then that $B^{\mathrm{off}}_{bs\tau,x} - i\tau B^{\mathrm{off}}_{bs\tau,y} = 0$ and $B^{\mathrm{off}}_{bs\tau,y} = -i\tau B^{\mathrm{off}}_{bs\tau,x}$, while $B^{\mathrm{off}}_{bs\tau,x} + i\tau B^{\mathrm{off}}_{bs\tau,y} = 2B^{\mathrm{off}}_{bs\tau,x}$. Therefore,

$$B^{\mathrm{off}}_{bs\tau,x} = \frac{3}{2}\sum_b \frac{|t_b(\tau\boldsymbol{K}^\theta)|^2}{E_{bs\tau}(\boldsymbol{k}'_1)^2} w_{bs\tau,\tau}(\boldsymbol{k}'_1) \tag{D14}$$

and $\delta H^{\mathrm{gr},\tau}_{As,Bs} = B^{\mathrm{off}}_{bs\tau,x}\tau\delta\boldsymbol{k}_x + B^{\mathrm{off}}_{bs\tau,y}\tau\delta\boldsymbol{k}_y = B^{\mathrm{off}}_{bs\tau,x}(\tau\delta\boldsymbol{k}_x - i\delta\boldsymbol{k}_y)$ as reported in Eq. (13).

APPENDIX E: ESTIMATION OF $t_\parallel$ AND $t_\perp$

According to Ref. [41] the value of $t_\perp$ for bilayer graphene is 110 meV. We expect $t_\perp$ for graphene–TMDC bilayers to be

of the same order of magnitude because the distance between graphene and the closest chalcogen layer is $d_\perp = 3.4$ Å [35] and happens to be equal to the distance reported between graphene layers [3]. For further comparison and in order to obtain the relative value of $t_\parallel$, we look at DFT calculations for graphene–TMDC heterostructures. Reference [33] reports an induced valley Zeeman spin-orbit splitting in graphene of -0.26 meV from the MoS_2 TMDC compound. This does not reveal immediately the values of $t_\parallel$ and $t_\perp$, but we can extract information about them using Eq. (12). Substituting Eq. (5) in Eq. (12), we expand the dependence of $|t_b|^2$ in $t_\parallel$ and $t_\perp$:

$$\lambda_{\mathrm{VZ}} = \alpha t_\parallel^2 + \beta t_\perp^2 + 2\gamma t_\parallel t_\perp, \tag{E1}$$

where

$$\begin{aligned}
\alpha &= 3\sum_b \frac{\widetilde{\alpha}\Delta_{0,b}(\boldsymbol{k}_1')}{E_b^2(\boldsymbol{k}_1') - \Delta_{0,b}^2(\boldsymbol{k}_1')},\\
\beta &= 3\sum_b \frac{\widetilde{\beta}\Delta_{0,b}(\boldsymbol{k}_1')}{E_b^2(\boldsymbol{k}_1') - \Delta_{0,b}^2(\boldsymbol{k}_1')},\\
\gamma &= 3\sum_b \frac{\widetilde{\gamma}\Delta_{0,b}(\boldsymbol{k}_1')}{E_b^2(\boldsymbol{k}_1') - \Delta_{0,b}^2(\boldsymbol{k}_1')}
\end{aligned} \tag{E2}$$

and

$$\begin{aligned}
\widetilde{\alpha} &= |c_{bx}(\tau\boldsymbol{k}_1')\cos\theta + c_{by}(\tau\boldsymbol{k}_1')\sin\theta|^2,\\
\widetilde{\beta} &= |c_{bz}(\tau\boldsymbol{k}_1')|^2,\\
\widetilde{\gamma} &= -\mathrm{Im}\{[c_{bx}(\tau\boldsymbol{k}_1')\cos\theta + c_{by}(\tau\boldsymbol{k}_1')\sin\theta]c_{bz}^*(\tau\boldsymbol{k}_1')\}.
\end{aligned} \tag{E3}$$

We see that α, β, and γ depend on the orbital amplitudes $c_{b,x,y,z}(\tau\boldsymbol{k}_1')$, the band dispersion $E_b(\boldsymbol{k}_1')$, and the spin splitting $\Delta_{0,b}(\boldsymbol{k}_1')$ which are intrinsic properties of the isolated TMDC layer and therefore can be readily calculated using the TB model of Ref. [50]. The only missing external parameter is the value of f_G which defines the distance of $E_b(\boldsymbol{k}_1')$ from the Dirac point. From Ref. [33], the Dirac point is very close to the conduction band of the TMDC and we set $f_G = 0.95$, meaning that the Dirac point of graphene has an energy distance from the TMDC conduction band edge equal to 5% of the TMDC band gap. We plug the resulting α, β, γ and the value of $\lambda_{\mathrm{VZ}} = -0.26$ meV in Eq. (E1) and the solutions for $t_\parallel$ and $t_\perp$ form an ellipse in the $(t_\parallel, t_\perp)$ plane (see Fig. 6). This ellipse is elongated and inclined by an angle of $\sim -40^\circ$. In principle, all the points $(t_\parallel, t_\perp)$ on this ellipse give $\lambda_{\mathrm{VZ}} = -0.26$ meV, but some values are unphysically large. Zooming closely to the center [see Fig. 6(b)], the ellipse touches the point $(t_\parallel, t_\perp) = (100, 100)$ meV. Since this is the order of magnitude that we expect, we estimate $t_\parallel \approx t_\perp \approx 100$ meV.

As presented at the end of Sec. VII, the results we obtain with these estimated values are in good qualitative agreement with previous works using DFT calculations [33] or TB models [40]. Nevertheless, it is possible that $t_\parallel$ and $t_\perp$ are overestimated. With the upper chalcogen layer approximation we have neglected the contribution coming from the d orbitals in order to simplify the treatment of the interlayer tunneling. In case the contribution of the d orbitals is significant, then $t_\parallel$ and $t_\perp$ would have a lower absolute value and the valley Zeeman SOC strength at zero twist angle, $\lambda_{\mathrm{VZ}} = -0.26$ meV, would be matched by additional radial integrals [see Eq. (B7)]

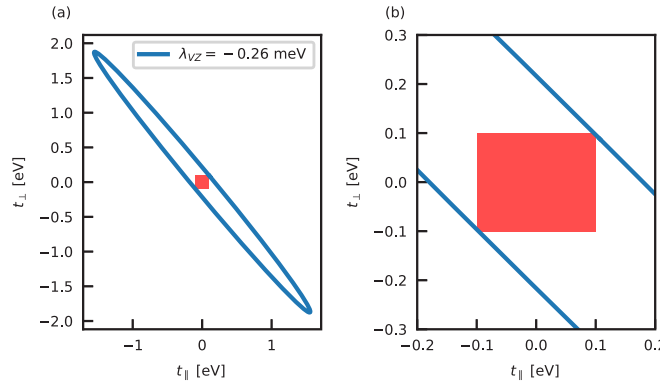

FIG. 6. Estimation of $t_\parallel$ and $t_\perp$. (a) The blue ellipse indicates the possible values of $t_\parallel$ and $t_\perp$ that give a valley Zeeman spin-orbit strength of -0.26 meV at $\theta = 0^\circ$ for a corresponding value of $f_G = 0.95$. (b) Magnification of (a). The red rectangle indicates the window of values where $|t_\parallel|, |t_\perp| \leqslant 100$ meV.

associated with the d orbitals. Thus, further research is needed to determine how relevant are the d orbitals in the interlayer tunneling.

APPENDIX F: RASHBA TYPE INDUCED SPIN-ORBIT COUPLING

In this Appendix we will show that the induced Rashba type SOC in graphene can be understood by taking into account spin-flip processes between even (e) and odd (o) bands of the TMDC. The energy bands of monolayer TMDCs can be classified as e or o under σ_h, which is the reflection with respect to the horizontal mirror plane of the TMDC.

Consider the following term in the effective low-energy Hamiltonian of graphene that can be obtained in third-order perturbation theory [53]:

$$\begin{aligned}
&\left(\delta H_R^{\mathrm{gr},\tau}\right)_{Xs,X's'}\\
&= \sum_{j,b,b',s'',s'''} \frac{\left(T_{\tau\boldsymbol{k}_j'}\right)_{Xs,bs''}(H_{\mathrm{soc}})_{bs'',b's'''}\left(T_{\tau\boldsymbol{k}_j'}^\dagger\right)_{b's''',X's'}}{\left[E_D^{\mathrm{gr}} - E_b^{\mathrm{TMDC}}(\tau\boldsymbol{k}_j')\right]\left[E_D^{\mathrm{gr}} - E_{b'}^{\mathrm{TMDC}}(\tau\boldsymbol{k}_j')\right]}.
\end{aligned} \tag{F1}$$

Here, $b \neq b'$ are band indices, and in the denominator we have neglected the dependence of the TMDC band energies $E_b^{\mathrm{TMDC}}(\tau\boldsymbol{k}_j')$ on the intrinsic SOC [cf. Eq. (10)] because it would lead to higher-order effects. Here, $(H_{\mathrm{soc}})_{bs'',b's'''}$ are matrix elements of the SOC operator

$$\hat{H}_{\mathrm{soc}} = \gamma_d \hat{\boldsymbol{L}}\cdot\hat{\boldsymbol{S}} = \gamma_d\left(\hat{L}_z\hat{S}_z + \tfrac{1}{2}(\hat{L}_+\hat{S}_- + \hat{L}_-\hat{S}_+)\right), \tag{F2}$$

which are nonzero only between e and o bands of the TMDC. Moreover, γ_d is the atomic SOC strength of the metal atoms' d orbitals, $\hat{L}_\pm = \hat{L}_x \pm i\hat{L}_y$, $\hat{L}_z$ are angular momentum operators, and $\hat{\boldsymbol{S}} = (\hat{S}_x, \hat{S}_y, \hat{S}_z)^T$, $\hat{S}_\pm = \hat{S}_x \pm i\hat{S}_y$ are spin operators, i.e., $\hat{\boldsymbol{S}} = (\hbar/2)\boldsymbol{s}$, where $\boldsymbol{s} = (s_x, s_y, s_z)^T$ are Pauli matrices. In order to show that Eq. (F1) describes Rashba type induced SOC, we focus, as a first step, on the matrix element between an even ($b = e$) and an odd ($b' = o$) band. At a general point

TABLE I. Matrix elements of the SOC operator in the basis of $\{d_{x^2-y^2}, d_{xy}, d_{z^2}, d_{xz}, d_{yz}\}$ atomic orbitals.

Orbital	d_{xz}	d_{yz}
d_{z^2}	$-i\sqrt{3}\hat{S}_y$	$i\sqrt{3}\hat{S}_x$
d_{xy}	$-i\hat{S}_x$	$i\hat{S}_y$
$d_{x^2-y^2}$	$i\hat{S}_y$	$i\hat{S}_x$

$\boldsymbol{k}'$ of the BZ the Bloch wave function of these bands can be written as

$$|e,\boldsymbol{k}'\rangle = c_{e,x^2-y^2}(\boldsymbol{k}')\,|d_{x^2-y^2},\boldsymbol{k}'\rangle + c_{e,xy}(\boldsymbol{k}')\,|d_{xy},\boldsymbol{k}'\rangle + c_{e,z^2}(\boldsymbol{k}')\,|d_{z^2},\boldsymbol{k}'\rangle\,, \tag{F3a}$$

$$|o,\boldsymbol{k}'\rangle = c_{o,xz}(\boldsymbol{k}')\,|d_{xz},\boldsymbol{k}'\rangle + c_{o,yz}(\boldsymbol{k}')\,|d_{yz},\boldsymbol{k}'\rangle\,, \tag{F3b}$$

where $|d_\mu,\boldsymbol{k}'\rangle$ are the usual Bloch wave functions formed using the d atomic orbitals of the metal atoms, $\mu \in \{x^2-y^2, xy, z^2, xz, yz\}$, and $c_{e\,(o),\mu}(\boldsymbol{k}')$ are complex amplitudes giving the weight of each type of atomic orbital at a given momentum space point. Other Bloch wave functions formed from the atomic orbitals $\{p_z, p_x, p_y\}$ of the chalcogen atoms have also finite weight in $|e\,(o),\boldsymbol{k}'\rangle$ and, as argued in previous sections, they are crucial to understand band-to-band tunneling. However, they are less important in the calculation of interband SOC matrix elements and therefore we do not take them into account explicitly in Eq. (F3). The interband spin matrices of $\hat{H}_{\rm soc}$ between these e and o bands can be written as

$$[H_{\rm soc}(\boldsymbol{k}')]_{e,o} = \langle e,\boldsymbol{k}'|\,\hat{H}_{\rm soc}\,|o,\boldsymbol{k}'\rangle = i\gamma_d\big[\alpha^{(x)}_{e,o}(\boldsymbol{k}')\hat{S}_x + \alpha^{(y)}_{e,o}(\boldsymbol{k}')\hat{S}_y\big], \tag{F4}$$

where $\alpha^{(x)}_{e,o} = (c_{e,x^2-y^2})^* c_{o,yz} - (c_{e,xy})^* c_{o,xz} + \sqrt{3}(c_{e,z^2})^* c_{o,yz}$ and $\alpha^{(y)}_{e,o} = (c_{e,x^2-y^2})^* c_{o,xz} + (c_{e,xy})^* c_{o,yz} - \sqrt{3}(c_{e,z^2})^* c_{o,xz}$ (for simplicity, we have suppressed the dependence of $\alpha^{(x,y)}_{e,o}$ on $\boldsymbol{k}'$, which will be restored later). Equation (F4) can be easily obtained by taking into account Table I. Note that $(H_{\rm soc})_{e,o}$ in Eq. (F4) has only off-diagonal nonzero elements in spin space $\uparrow,\downarrow$, i.e., it describes spin-flip processes between the two bands. The term that would be $\sim\hat{S}_z$ vanishes between e and o bands by symmetry.

As one can see from Eq. (F1), one needs to calculate $(H_{\rm soc})_{es'',os'''}$ at the three $\boldsymbol{k}'_j$ BZ points of the TMDC defined in Eq. (4) that satisfy the quasimomentum conservation for interlayer tunneling. These points are related to each other by a $2\pi/3$ rotation. Following Ref. [61], we may write $|e\,(o), R_{\pm2\pi/3}\boldsymbol{k}'_1\rangle = R_{\pm2\pi/3}\,|e\,(o),\boldsymbol{k}'_1\rangle$, where $R_{\pm2\pi/3}$ denotes rotation by $\pm2\pi/3$. Therefore, given $\langle e,\boldsymbol{k}'_1|\,\hat{H}_{\rm soc}\,|o,\boldsymbol{k}'_1\rangle$, one needs to evaluate

$$\langle e, R_{2\pi/3}\boldsymbol{k}'_1|\,\hat{H}_{\rm soc}\,|o, R_{2\pi/3}\boldsymbol{k}'_1\rangle = \langle e,\boldsymbol{k}'_1|\,(R_{2\pi/3})^\dagger\,\hat{H}_{\rm soc}\,R_{2\pi/3}\,|o,\boldsymbol{k}'_1\rangle\,, \tag{F5a}$$

$$\langle e, R_{-2\pi/3}\boldsymbol{k}'_1|\,\hat{H}_{\rm soc}\,|o, R_{-2\pi/3}\boldsymbol{k}'_1\rangle = \langle e,\boldsymbol{k}'_1|\,(R_{-2\pi/3})^\dagger\,\hat{H}_{\rm soc}\,R_{-2\pi/3}\,|o,\boldsymbol{k}'_1\rangle\,. \tag{F5b}$$

This means that the necessary matrix elements can be calculated using $|e,\boldsymbol{k}'_1\rangle$ and $|o,\boldsymbol{k}'_1\rangle$ and a rotated $\hat{H}_{\rm soc}$. The transformed operators $(R_{\pm2\pi/3})^\dagger\hat{H}_{\rm soc}R_{\pm2\pi/3}$ can be easily calculated by noticing that

$$(R_{\pm2\pi/3})^\dagger\,\hat{L}_z\,R_{\pm2\pi/3} = \hat{L}_z, \tag{F6a}$$

$$R_{2\pi/3}\,\hat{L}_\pm\,(R_{2\pi/3})^\dagger = e^{\mp i2\pi/3}\hat{L}_\pm, \tag{F6b}$$

$$R_{-2\pi/3}\,\hat{L}_\pm\,(R_{-2\pi/3})^\dagger = e^{\pm i2\pi/3}\hat{L}_\pm. \tag{F6c}$$

Let us define the vectors $\boldsymbol{n}_{e,o}(\boldsymbol{k}'_1) = (\alpha^{(x)}_{e,o}(\boldsymbol{k}'_1), \alpha^{(y)}_{e,o}(\boldsymbol{k}'_1))^T$, $\boldsymbol{S} = (S_x, S_y)^T$. Then, one finds that

$$[H_{\rm soc}(\boldsymbol{k}'_1)]_{e,o} = i\gamma_d\,\boldsymbol{n}_{e,o}(\boldsymbol{k}'_1)\cdot\boldsymbol{S}, \tag{F7a}$$

$$[H_{\rm soc}(R_{2\pi/3}\boldsymbol{k}'_1)]_{e,o} = i\gamma_d(R_{2\pi/3}\boldsymbol{n}_{e,o}(\boldsymbol{k}'_1))\cdot\boldsymbol{S}, \tag{F7b}$$

$$[H_{\rm soc}(R_{-2\pi/3}\boldsymbol{k}'_1)]_{e,o} = i\gamma_d(R_{-2\pi/3}\boldsymbol{n}_{e,o}(\boldsymbol{k}'_1))\cdot\boldsymbol{S}. \tag{F7c}$$

Note that $\boldsymbol{n}_{e,o}(\boldsymbol{k}'_1)$ in Eqs. (F7) is in general a complex vector because the weights $c_{e\,(o),\mu}(\boldsymbol{k}'_1)$ of the atomic orbitals in band e (o) can be complex.

We can compute now the contribution to $\delta H^{\rm gr,\tau}_R$ from the interaction of two bands of the TMDC (e.g., the conduction band which is e and the first o band above the conduction band). Then, the indices b and b' in Eq. (F1) can take the values $(b,b') = (e,o)$ and $(b,b') = (o,e)$. For simplicity, we focus on the Dirac point $\boldsymbol{K}$, i.e., $\tau = 1$. Note that the energy differences $[E^{\rm gr}_D - E^{\rm TMDC}_b(\boldsymbol{k}'_j)]$ and $[E^{\rm gr}_D - E^{\rm TMDC}_{b'}(\boldsymbol{k}'_j)]$ appearing in Eq. (F1) are equal for all $\boldsymbol{k}'_j$ because of the threefold rotational (C_3) symmetry of the TMDC. Therefore, the corresponding factor can be pulled out of the sum in Eq. (F1). Using Eq. (9) one may write explicitly

$$\begin{aligned}\delta H^{\rm gr}_R = \frac{1}{\big[E^{\rm gr}_D - E^{\rm TMDC}_e(\boldsymbol{k}'_1)\big]\big[E^{\rm gr}_D - E^{\rm TMDC}_o(\boldsymbol{k}'_1)\big]}\Bigg[&\begin{pmatrix}1 & 1\\ 1 & 1\end{pmatrix}\otimes[T_{e,o}[H_{\rm soc}(\boldsymbol{k}'_1)]_{e,o} + T_{o,e}[H_{\rm soc}(\boldsymbol{k}'_1)]_{o,e}]\\ &+\begin{pmatrix}1 & e^{-2i\pi/3}\\ e^{2i\pi/3} & 1\end{pmatrix}\otimes[T_{e,o}[H_{\rm soc}(R_{2\pi/3}\boldsymbol{k}'_1)]_{e,o} + T_{o,e}[H_{\rm soc}(R_{2\pi/3}\boldsymbol{k}'_1)]_{o,e}]\\ &+\begin{pmatrix}1 & e^{2i\pi/3}\\ e^{-2i\pi/3} & 1\end{pmatrix}\otimes[T_{e,o}[H_{\rm soc}(R_{-2\pi/3}\boldsymbol{k}'_1)]_{e,o} + T_{o,e}[H_{\rm soc}(R_{-2\pi/3}\boldsymbol{k}'_1)]_{o,e}]\Bigg].\end{aligned} \tag{F8}$$

Here, $T_{e,o} = t_e(\boldsymbol{K}^\theta)t_o^*(\boldsymbol{K}^\theta)$ where $t_b(\boldsymbol{K}^\theta)$ is given in Eq. (5), $T_{o,e} = T_{e,o}^*$, and $[H_{\rm soc}(\boldsymbol{k}')]_{o,e} = [H_{\rm soc}(\boldsymbol{k}')]_{e,o}^\dagger$. Let us write $T_{e,o} = |T_{e,o}|e^{i\eta}$, then using Eqs. (F7)

$$\begin{aligned} T_{e,o}[H_{\rm soc}(\boldsymbol{k}_1')]_{e,o} + T_{e,o}^*[H_{\rm soc}(\boldsymbol{k}_1')]_{e,o}^\dagger &= i\gamma_d|T_{e,o}|[e^{i\eta}\boldsymbol{n}_{e,o}(\boldsymbol{k}_1') - e^{-i\eta}(\boldsymbol{n}_{e,o})^*(\boldsymbol{k}_1')]\cdot\boldsymbol{S} \\ &= -2\gamma_d|T_{e,o}|(\mathrm{Im}[e^{i\eta}\boldsymbol{n}_{e,o}(\boldsymbol{k}_1')])\cdot\boldsymbol{S} \\ &= 2i\gamma_d|T_{e,o}|\begin{pmatrix} 0 & \Lambda_2(\boldsymbol{k}_1') \\ \Lambda_1(\boldsymbol{k}_1') & 0 \end{pmatrix}, \end{aligned} \tag{F9a}$$

$$\begin{aligned} T_{e,o}[H_{\rm soc}(R_{2\pi/3}\boldsymbol{k}_1')]_{e,o} + T_{e,o}^*[H_{\rm soc}(R_{2\pi/3}\boldsymbol{k}_1')]_{e,o}^\dagger &= -2\gamma_d|T_{e,o}|(R_{2\pi/3}\,\mathrm{Im}[e^{i\eta}\boldsymbol{n}_{e,o}(\boldsymbol{k}_1')])\cdot\boldsymbol{S} \\ &= 2i\gamma_d|T_{e,o}|\begin{pmatrix} 0 & e^{-2i\pi/3}\Lambda_2(\boldsymbol{k}_1') \\ e^{2i\pi/3}\Lambda_1(\boldsymbol{k}_1') & 0 \end{pmatrix}, \end{aligned} \tag{F9b}$$

$$\begin{aligned} T_{e,o}[H_{\rm soc}(R_{-2\pi/3}\boldsymbol{k}_1')]_{e,o} + T_{e,o}^*[H_{\rm soc}(R_{-2\pi/3}\boldsymbol{k}_1')]_{e,o}^\dagger &= -2\gamma_d|T_{e,o}|(R_{-2\pi/3}\,\mathrm{Im}[e^{i\eta}\boldsymbol{n}_{e,o}(\boldsymbol{k}_1')])\cdot\boldsymbol{S} \\ &= 2i\gamma_d|T_{e,o}|\begin{pmatrix} 0 & e^{2i\pi/3}\Lambda_2(\boldsymbol{k}_1') \\ e^{-2i\pi/3}\Lambda_1(\boldsymbol{k}_1') & 0 \end{pmatrix}. \end{aligned} \tag{F9c}$$

Here, $\Lambda_1(\boldsymbol{k}_1') = -\mathrm{Im}[e^{i\eta}\alpha_{e,o}^{(y)}(\boldsymbol{k}_1')] + i\,\mathrm{Im}[e^{i\eta}\alpha_{e,o}^{(x)}(\boldsymbol{k}_1')]$ and $\Lambda_2(\boldsymbol{k}_1') = \mathrm{Im}[e^{i\eta}\alpha_{e,o}^{(y)}(\boldsymbol{k}_1')] + i\,\mathrm{Im}[e^{i\eta}\alpha_{e,o}^{(x)}(\boldsymbol{k}_1')]$. Note that one can write $\Lambda_1(\boldsymbol{k}_1') = |\Lambda_1(\boldsymbol{k}_1')|e^{i\vartheta(\boldsymbol{k}_1')}$ and $\Lambda_2(\boldsymbol{k}_1') = -|\Lambda_1(\boldsymbol{k}_1')|e^{-i\vartheta(\boldsymbol{k}_1')}$ where $\vartheta(\boldsymbol{k}_1') = \mathrm{Arg}[\Lambda_1(\boldsymbol{k}_1')]$. Substituting now Eqs. (F9) into Eq. (F8) one finds

$$\delta H_R^{gr} = \begin{pmatrix} 0 & 0 & 0 & 0 \\ 0 & 0 & i\lambda_R(\boldsymbol{k}_1')e^{i\vartheta(\boldsymbol{k}_1')} & 0 \\ 0 & -i\lambda_R(\boldsymbol{k}_1')e^{-i\vartheta(\boldsymbol{k}_1')} & 0 & 0 \\ 0 & 0 & 0 & 0 \end{pmatrix}, \tag{F10}$$

where

$$\lambda_R(\boldsymbol{k}_1') = \frac{6\gamma_d|T_{e,o}(\boldsymbol{k}_1')||\Lambda_1(\boldsymbol{k}_1')|}{\left[E_D^{\rm gr} - E_e^{\rm TMDC}(\boldsymbol{k}_1')\right]\left[E_D^{\rm gr} - E_o^{\rm TMDC}(\boldsymbol{k}_1')\right]}. \tag{F11}$$

Equation (F11) is the strength of the Rashba type SOC induced in graphene by each pair of e and o bands. As Eq. (F1) shows, in order to calculate the total spin-orbit coupling $\lambda_R(\boldsymbol{k}_1')$ one needs to sum up the contributions coming from all pairs of even and odd bands with the correct phase factors shown in Eq. (F10). A similar result to Eq. (F10) can be obtained in an analogous way for the opposite Dirac point $-\boldsymbol{K}$.

[1] K. S. Novoselov, A. K. Geim, S. V. Morozov, D. Jiang, Y. Zhang, S. V. Dubonos, I. V. Grigorieva, and A. A. Firsov, Science **306**, 666 (2004).

[2] K. S. Novoselov, A. K. Geim, S. V. Morozov, D. Jiang, M. I. Katsnelson, I. V. Grigorieva, S. V. Dubonos, and A. A. Firsov, Nature (London) **438**, 197 (2005).

[3] A. H. Castro Neto, F. Guinea, N. M. R. Peres, K. S. Novoselov, and A. K. Geim, Rev. Mod. Phys. **81**, 109 (2009).

[4] M. Drögeler, C. Franzen, F. Volmer, T. Pohlmann, L. Banszerus, M. Wolter, K. Watanabe, T. Taniguchi, C. Stampfer, and B. Beschoten, Nano Lett. **16**, 3533 (2016).

[5] S. Singh, J. Katoch, J. Xu, C. Tan, T. Zhu, W. Amamou, J. Hone, and R. Kawakami, Appl. Phys. Lett. **109**, 122411 (2016).

[6] J. Ingla-Aynés, M. H. D. Guimarães, R. J. Meijerink, P. J. Zomer, and B. J. van Wees, Phys. Rev. B **92**, 201410(R) (2015).

[7] W. Han, R. K. Kawakami, M. Gmitra, and J. Fabian, Nat. Nanotechnol. **9**, 794 (2014).

[8] M. Gmitra, S. Konschuh, C. Ertler, C. Ambrosch-Draxl, and J. Fabian, Phys. Rev. B **80**, 235431 (2009).

[9] C. L. Kane and E. J. Mele, Phys. Rev. Lett. **95**, 226801 (2005).

[10] T. Frank, P. Högl, M. Gmitra, D. Kochan, and J. Fabian, Phys. Rev. Lett. **120**, 156402 (2018).

[11] A. K. Geim and I. V. Grigorieva, Nature (London) **499**, 419 (2013).

[12] A. Avsar, J. Y. Tan, T. Taychatanapat, J. Balakrishnan, G. K. W. Koon, Y. Yeo, J. Lahiri, A. Carvalho, A. S. Rodin, E. C. T. O'Farrell, G. Eda, A. H. Castro Neto, and B. Özyilmaz, Nat. Commun. **5**, 4875 (2014).

[13] Z. Wang, D.-K. Ki, H. Chen, H. Berger, A. H. MacDonald, and A. F. Morpurgo, Nat. Commun. **6**, 8339 (2015).

[14] Z. Wang, D.-K. Ki, J. Y. Khoo, D. Mauro, H. Berger, L. S. Levitov, and A. F. Morpurgo, Phys. Rev. X **6**, 041020 (2016).

[15] B. Yang, M.-F. Tu, J. Kim, Y. Wu, H. Wang, J. Alicea, R. Wu, M. Bockrath, and J. Shi, 2D Mater. **3**, 031012 (2016).

[16] W. Yan, O. Txoperena, R. Llopis, H. Dery, L. E. Hueso, and F. Casanova, Nat. Commun. **7**, 13372 (2016).

[17] B. Yang, M. Lohmann, D. Barroso, I. Liao, Z. Lin, Y. Liu, L. Bartels, K. Watanabe, T. Taniguchi, and J. Shi, Phys. Rev. B **96**, 041409(R) (2017).

[18] T. S. Ghiasi, J. Ingla-Aynés, A. A. Kaverzin, and B. J. van Wees, Nano Lett. **17**, 7528 (2017).

[19] A. Dankert and S. P. Dash, Nat. Commun. **8**, 16093 (2017).

[20] T. Völkl, T. Rockinger, M. Drienovsky, K. Watanabe, T. Taniguchi, D. Weiss, and J. Eroms, Phys. Rev. B **96**, 125405 (2017).

[21] S. Zihlmann, A. W. Cummings, J. H. Garcia, M. Kedves, K. Watanabe, T. Taniguchi, C. Schönenberger, and P. Makk, Phys. Rev. B **97**, 075434 (2018).

[22] T. Wakamura, F. Reale, P. Palczynski, S. Guéron, C. Mattevi, and H. Bouchiat, Phys. Rev. Lett. **120**, 106802 (2018).

[23] J. C. Leutenantsmeyer, J. Ingla-Aynés, J. Fabian, and B. J. van Wees, Phys. Rev. Lett. **121**, 127702 (2018).

[24] S. Omar and B. J. van Wees, Phys. Rev. B **97**, 045414 (2018).

[25] L. A. Benítez, J. F. Sierra, W. S. Torres, A. Arrighi, F. Bonell, M. V. Costache, and S. O. Valenzuela, Nat. Phys. **14**, 303 (2018).

[26] C. K. Safeer, J. Ingla-Aynés, F. Herling, J. H. Garcia, M. Vila, N. Ontoso, M. R. Calvo, S. Roche, L. E. Hueso, and F. Casanova, Nano Lett. **19**, 1074 (2019).

[27] A. V. Kretinin, Y. Cao, J. S. Tu, G. L. Yu, R. Jalil, K. S. Novoselov, S. J. Haigh, A. Gholinia, A. Mishchenko, M. Lozada, T. Georgiou, C. R. Woods, F. Withers, P. Blake, G. Eda, A. Wirsig, C. Hucho, K. Watanabe, T. Taniguchi, A. K. Geim, and R. V. Gorbachev, Nano Lett. **14**, 3270 (2014).

[28] A. Kormányos, G. Burkard, M. Gmitra, J. Fabian, V. Zólyomi, N. D. Drummond, and Vladimir Fal'ko, 2D Mater. **2**, 022001 (2015).

[29] J. H. Garcia, M. Vila, A. W. Cummings, and S. Roche, Chem. Soc. Rev. **47**, 3359 (2018).

[30] A. W. Cummings, J. H. Garcia, J. Fabian, and S. Roche, Phys. Rev. Lett. **119**, 206601 (2017).

[31] T. P. Kaloni, L. Kou, T. Frauenheim, and U. Schwingenschlögl, Appl. Phys. Lett. **105**, 233112 (2014).

[32] M. Gmitra and J. Fabian, Phys. Rev. B **92**, 155403 (2015).

[33] M. Gmitra, D. Kochan, P. Högl, and J. Fabian, Phys. Rev. B **93**, 155104 (2016).

[34] S. Singh, A. M. Alsharari, S. E. Ulloa, and A. H. Romero, in *Handbook of Graphene: Graphene-like 2D Materials*, edited by M. Zhang (Wiley-Scrivener, New York, 2019), Chap. 1.

[35] D. Pierucci, H. Henck, J. Avila, A. Balan, C. H. Naylor, G. Patriarche, Y. J. Dappe, M. G. Silly, F. Sirotti, A. T. C. Johnson, M. C. Asensio, and A. Ouerghi, Nano Lett. **16**, 4054 (2016).

[36] Z. Wang, Q. Chen, and J. Wang, J. Phys. Chem. C **119**, 4752 (2015).

[37] D. D. Felice, E. Abad, C. González, A. Smogunov, and Y. J. Dappe, J. Phys. D: Appl. Phys. **50**, 17LT02 (2017).

[38] A. M. Alsharari, M. M. Asmar, and S. E. Ulloa, Phys. Rev. B **94**, 241106(R) (2016).

[39] A. M. Alsharari, M. M. Asmar, and S. E. Ulloa, Phys. Rev. B **98**, 195129 (2018)

[40] Y. Li and M. Koshino, Phys. Rev. B **99**, 075438 (2019).

[41] R. Bistritzer and A. H. MacDonald, Proc. Natl. Acad. Sci. U. S. A. **108**, 12233 (2011).

[42] S. Carr, D. Massatt, S. Fang, P. Cazeaux, M. Luskin, and E. Kaxiras, Phys. Rev. B **95**, 075420 (2017).

[43] Y. Cao, V. Fatemi, S. Fang, K. Watanabe, T. Taniguchi, E. Kaxiras, and P. Jarillo-Herrero, Nature (London) **556**, 43 (2018).

[44] R. Ribeiro-Palau, C. Zhang, K. Watanabe, T. Taniguchi, J. Hone, and C. R. Dean, Science **361**, 690 (2018).

[45] K. F. Mak, C. Lee, J. Hone, J. Shan, and T. F. Heinz, Phys. Rev. Lett. **105**, 136805 (2010).

[46] A. Splendiani, L. Sun, Y. Zhang, T. Li, J. Kim, C.-Y. Chim, G. Galli, and F. Wang, Nano Lett. **10**, 1271 (2010).

[47] M. Koshino, New J. Phys. **17**, 015014 (2015).

[48] R. Bistritzer and A. H. MacDonald, Phys. Rev. B **81**, 245412 (2010).

[49] J. C. Slater and G. F. Koster, Phys. Rev. **94**, 1498 (1954).

[50] S. Fang, R. Kuate Defo, S. N. Shirodkar, S. Lieu, G. A. Tritsaris, and E. Kaxiras, Phys. Rev. B **92**, 205108 (2015).

[51] J. R. Schrieffer and P. A. Wolff, Phys. Rev. **149**, 491 (1966).

[52] S. Bravyi, D. P. DiVincenzo, and D. Loss, Ann. Phys. **326**, 2793 (2011).

[53] R. Winkler, *Spin–Orbit Coupling Effects in Two-Dimensional Electron and Hole Systems*, Springer Tracts in Modern Physics, Vol. 191 (Springer, Berlin, 2003).

[54] C. Hwang, D. A. Siegel, S.-K. Mo, W. Regan, A. Ismach, Y. Zhang, A. Zettl, and A. Lanzara, Sci. Rep. **2**, 590 (2012).

[55] H. Min, J. E. Hill, N. A. Sinitsyn, B. R. Sahu, L. Kleinman, and A. H. MacDonald, Phys. Rev. B **74**, 165310 (2006).

[56] A. Kormányos, V. Zólyomi, N. D. Drummond, and G. Burkard, Phys. Rev. X **4**, 011034 (2014).

[57] J. Sichau, M. Prada, T. Anlauf, T. J. Lyon, B. Bosnjak, L. Tiemann, and R. H. Blick, Phys. Rev. Lett. **122**, 046403 (2019).

[58] S. Ilić, J. S. Meyer, and M. Houzet, Phys. Rev. B **99**, 205407 (2019).

[59] D. Colton and R. Kress, *Inverse Acoustic and Electromagnetic Scattering Theory*, 2nd ed., Applied Mathematical Sciences (Springer, Berlin, 1998).

[60] A. A. M. Cuyt, V. Petersen, B. Verdonk, H. Waadeland, and W. B. Jones, *Handbook of Continued Fractions for Special Functions* (Springer, Dordrecht, 2008).

[61] M. S. Dresselhaus, G. Dresselhaus, and A. Jorio, *Group Theory: Application to the Physics of Condensed Matter* (Springer, Berlin, 2010).